PHYSICAL REVIEW E **95**, 032802 (2017)

Tricritical Casimir forces and order parameter profiles in wetting films of ^{3}He-^{4}He mixtures

N. Farahmand Bafi,[1,2,*] A. Maciołek,[3,1,†] and S. Dietrich[1,2,‡]
[1]*Max-Planck-Institut für Intelligente Systeme, Heisenbergstr. 3, D-70569 Stuttgart, Germany*
[2]*Institut für Theoretische Physik IV, Universität Stuttgart, Pfaffenwaldring 57, D-70569 Stuttgart, Germany*
[3]*Institute of Physical Chemistry, Polish Academy of Sciences, Kasprzaka 44/52, PL-01-224 Warsaw, Poland*

(Received 23 November 2016; published 13 March 2017)

Tricritical Casimir forces in ^{3}He-^{4}He wetting films are studied, within mean field theory, in terms of a suitable lattice gas model for binary liquid mixtures with short-ranged surface fields. The proposed model takes into account the continuous rotational symmetry O(2) of the superfluid degrees of freedom associated with ^{4}He and it allows, *inter alia*, for the occurrence of a vapor phase. As a result, the model facilitates the formation of wetting films, which provides a strengthened theoretical framework to describe available experimental data for tricritical Casimir forces acting in ^{3}He-^{4}He wetting films.

DOI: 10.1103/PhysRevE.95.032802

I. INTRODUCTION

Concerning fluid wetting films near a critical point [1], experimental studies have provided convincing evidence for a long-ranged effective interaction emerging between the planar solid surface and the parallel fluid interface forming the film [2–8]. Such fluid-mediated and fluctuation induced interactions were discussed first by Fisher and de Gennes [9] on the basis of finite-size scaling [10,11] for critical binary liquid mixtures. They are known as *critical Casimir forces* (CCFs) in analogy with the well-known Casimir forces in quantum electrodynamics [12,13]. In wetting films of a classical binary liquid mixture, within its bulk phase diagram the CCF arises near the critical end point of the liquid mixture, at which the line of critical points of the liquid-liquid demixing transitions encounters the liquid-vapor coexistence surface [1,14]. They originate from the restriction and modification of the critical fluctuations of the composition of the mixture imposed on one side by the solid substrate and on the other side by the emerging liquid-vapor interface. The CCF acts by moving the liquid-vapor interface, and, together with the omnipresent background dispersion forces and gravity, it determines the equilibrium thickness ℓ of the wetting films [5–8]. The dependence of ℓ on temperature T provides an indirect measurement of CCF [1,14]. This approach also allows one to probe the universal properties of the CCF encoded in its scaling function [1]. By varying the undersaturation of the vapor phase one can tune the film thickness and thus determine the scaling behavior of the CCF as function of T and ℓ [1,15,16]. The shape of such a universal scaling function depends on the bulk universality class of the confined fluid and on the surface universality classes of the two confining boundaries [17]. The latter are related to the boundary conditions (BCs) [13,17,18] imposed by the surfaces on the order parameter (OP) associated with the underlying second-order phase transition [18]. In general, the scaling function of CCFs is negative (attractive CCFs) for symmetric BCs and positive (repulsive CCFs) for nonsymmetric ones. Classical binary liquid mixtures near their demixing transition belong to the three-dimensional Ising universality class. The surfaces confining them belong to the so-called normal transition [17], which is characterized by a strong effective surface field acting on the deviation of the concentration from its critical value serving as the OP. The surface field describes the preference of the surface for one of the two species forming the binary liquid mixture. Since the two surfaces typically exhibit opposite preferences, wetting films of classical binary liquid mixtures are often characterized by opposing surface fields [$(+,-)$ BCs], which results in repulsive CCFs [5–8].

In wetting films of ^{4}He [2], the CCF originates from the confined critical fluctuations associated with the continuous superfluid phase transition along the so-called λ line. Similarly as for the classical binary liquid mixtures, here the CCF emerges near that critical end point where the λ line encounters the line of first-order liquid-vapor phase transitions of ^{4}He.

Capacitance measurements of the equilibrium thickness of ^{4}He wetting films have provided strong evidence for an attractive CCF [2,4] in quantitative agreement with the theoretical predictions [1,16] for the corresponding bulk XY universality class with *symmetric* Dirichlet-Dirichlet BCs (O,O), which correspond to the vanishing of the superfluid OP with O(2) symmetry both at the surface of the substrate and at the liquid-vapor interface. The scaling function of this CCF has, to a certain extent, been determined analytically [1,16,19–22] and by using Monte Carlo simulations [23–28]. Their results are in excellent agreement with the experimental data.

Similar measurements [3] for wetting films of ^{3}He-^{4}He mixtures performed near the tricritical end point, at which the line of tricritical points encounters the sheet of first-order liquid-vapor phase transitions (see the phase diagram of ^{3}He-^{4}He mixtures in Fig. 1), revealed a repulsive tricritical Casimir force (TCF). In turn this points towards nonsymmetric BCs for the superfluid OP, which is surprising because in this system there are no surface fields which couple to the superfluid OP. However, there is a subtle physical mechanism which can create $(+,O)$ and thus nonsymmetric BCs. As argued in Ref. [3], the ^{3}He isotope is lighter than ^{4}He and thus experiences a larger zero-point motion. Hence it occupies a larger volume than ^{4}He. As a result, ^{3}He atoms are effectively expelled from the rigid solid substrate and tend to gather at the soft liquid-vapor interface. This leads to an effective attraction of ^{4}He atoms to the solid substrate so that a ^{4}He-rich

---

[*] nimabafi@is.mpg.de

[†] maciolek@is.mpg.de

[‡] dietrich@is.mpg.de

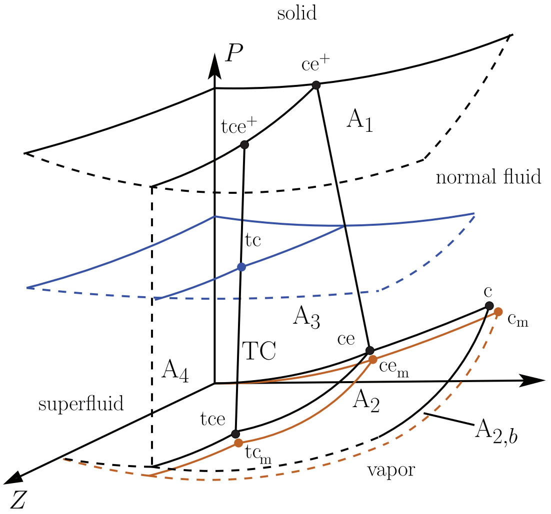

FIG. 1. Schematic bulk phase diagram of ^{3}He-^{4}He mixtures (black curves and surfaces) and two specific surfaces (blue and brown) in the (T,Z,P) space, where P is the pressure and $Z = \exp(\mu_3/T)$ is the fugacity of ^{3}He, with μ_3 as the chemical potential of ^{3}He atoms [1]. A_1 shows the surface of first-order solid-liquid phase transitions, whereas A_2 is the surface of first-order vapor-liquid phase transitions. The phase transitions between the normal fluid and the superfluid phase are either of second or of first order, which are shown by the surfaces A_3 and A_4, respectively. The surfaces A_3 and A_1 intersect along a line ce$^+$-tce$^+$ of critical end points. The surfaces A_3 and A_4 are separated by a line tce$^+$-tce of tricritical points TC. This line meets A_1 and A_2 at the tricritical end points tce$^+$ and tce, respectively. The surfaces A_3 and A_2 intersect along a line ce-tce of critical end points. The surface A_2 terminates at a line of critical points, starting from c in the plane $Z = 0$. The phase diagram in the plane $Z = 0$ corresponds to that of pure ^{4}He. The dashed lines indicate that the corresponding surface continues. On the blue surface the total density is constant, which corresponds to the situation studied in Refs. [20,21]. The brown surface $A_{2,b}$ lies in the vapor phase slightly below the liquid-vapor coexistence surface A_2. Although the thermodynamic fields along the thermodynamic paths taken in the experiment in Ref. [3] have been tuned to their values at the liquid-vapor coexistence surface, due to gravity the actual measurements have been carried out for thermodynamic states which lie on a surface resembling the brown one. At the thermodynamic states on the brown surface, in addition to the stable vapor phase, there are metastable liquid phases. These metastable liquid phases undergo transitions similar to the liquid-liquid phase transitions tied to A_2. Therefore, for each point tce, ce, and c, there is a metastable counterpart tc$_\mathrm{m}$, ce$_\mathrm{m}$, and c$_\mathrm{m}$, respectively, on the brown surface.

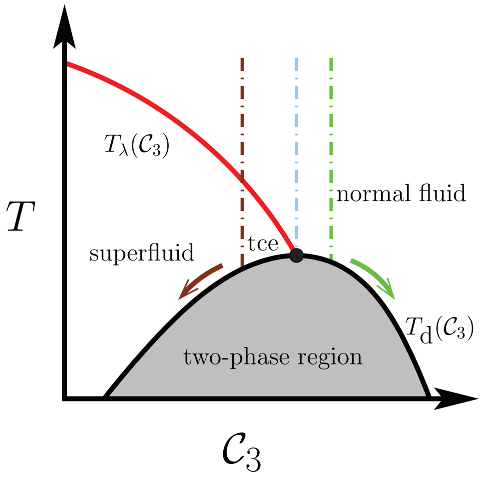

FIG. 2. Liquid-liquid bulk phase transitions at coexistence with the vapor phase for ^{3}He-^{4}He mixtures and the thermodynamic paths taken in the experiments reported in Ref. [3]. The black curves denote the first-order phase transitions between the normal fluid phase and the superfluid phase, which terminate at the tricritical end point tce. The red curve shows the second-order λ transitions between the normal fluid phase and the superfluid phase. The dashed dotted lines indicate three distinct thermodynamic paths corresponding to three fixed values of the concentration $\mathcal{C}_3 = X_3/(X_3 + X_4)$ [see, cf., Eq. (17)] of the ^{3}He atoms as done experimentally. X_3 and X_4 are the bulk number densities of ^{3}He and ^{4}He, respectively. Upon decreasing the temperature, the bulk liquid undergoes a first-order phase separation at some demixing temperature $T_\mathrm{d}(\mathcal{C}_3)$. Upon further decrease of the temperature the thermodynamic paths follow that branch of the coexistence curve, which they hit (see the the brown and green arrows).

layer forms near the substrate-liquid interface, which due to the increased ^{4}He concentration may become superfluid at temperatures already above the line of onset of superfluidity in the bulk [29]. Thus the two interfaces impose a nontrivial concentration profile across the film, which in turn couples to the superfluid OP. Explicit calculations [20,21] within the vectorized Blume-Emery-Griffiths (VBEG) model of helium mixtures [30–32] have demonstrated that the concentration profile indeed induces indirectly nonsymmetric BCs for the superfluid OP. A semiquantitative agreement with the experimental data given in Ref. [3] has been found for the TCF, computed by assuming a symmetry-breaking (+) BC at the substrate-liquid interface and a Dirichlet (O) BC at the liquid-vapor interface. However, the VBEG model employed in Refs. [20,21] does not incorporate the vapor phase and hence cannot exhibit wetting films. In these studies the confinement of the liquid between the substrate and the liquid-vapor interface has been modeled by a slab geometry with the boundaries introduced by fiat, mimicking the actual self-consistent formation of wetting films and thus differing from the actual experimental setup. This difference is borne out in Fig. 1. Therein the surface of constant total density $D(P,T,Z) = \text{const}$ is shown in blue. The analyses in Refs. [20,21] have been carried out within such a surface, whereas the experiment in Ref. [3] has been carried out along the surface of liquid-vapor coexistence. Note that, although the thermodynamic states, for which the measurements have been performed, correspond to the liquid-vapor coexistence surface (surface A_2 in Fig. 1), due to gravity the actual thermodynamic paths lie on a surface, which is located slightly in the vapor phase (brown surface in Fig. 1). Figures 2 and 3 show these thermodynamic paths.

In order to pave the way for providing a more realistic description of the experimental setup reported in Ref. [3], recently we have extended the VBEG model such that the vapor phase is incorporated into the phase diagram [33]. We have found that allowing for the corresponding vacancies in the lattice model leads to a rich phase behavior in the bulk with complex phase diagrams of various topologies. We were

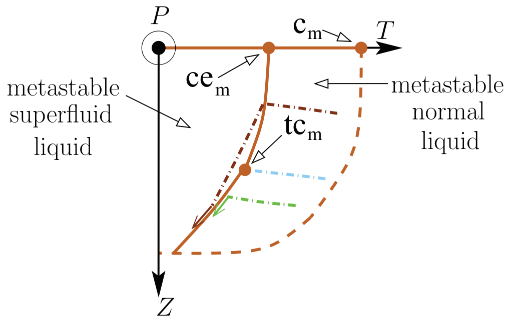

FIG. 3. Projection of the brown surface $A_{2,b}$ in Fig. 1 (which lies in the vapor phase) onto the (P,T) plane. The solid and dashed brown lines are the projections of the corresponding ones for $A_{2,b}$. The dashed-dotted lines are the projections of the thermodynamic paths shown in Fig. 2 and which lie on the brown surface. Upon lowering T the brown dashed-dotted line first crosses the full line $T_\lambda(\mathcal{C}_3)$ in Fig. 2, continues through the superfluid phase and then encounters the two-phase region. This sketch is based on our numerical results (see Sec. III B) in the vicinity of tc_m.

able to determine that range of interaction parameters for which the bulk phase diagram resembles the one observed experimentally for ^{3}He-^{4}He mixtures, i.e., for which first-order demixing ends via a tricritical point at the λ line of second-order superfluid transitions [33]. In the present study, we use this model in order to describe wetting of a solid substrate by ^{3}He-^{4}He mixtures. We analyze the behavior of the wetting films along the thermodynamic paths corresponding to the ones in the experiment [3]. This will allow us to compare the variation of the wetting film thickness with the experimental data shown in Fig. 14 of Ref. [3] (see Sec. III), which is not possible within the approach used in Refs. [20,21]. Finally, we aim at extracting the TCF contribution to the effective force between the solid substrate and the emerging liquid-vapor interface. We shall compare its scaling function with that extracted from the experimental data in Ref. [3] and the one calculated using the simple slab geometry employed in Refs. [20,21]. We study our model in spatial dimension $d = 3$ within mean field theory, which, up to logarithmic corrections, captures the universal behavior of the TCF near the tricritical point of ^{4}He -^{4}He mixtures. However, this approximation is insufficient near the critical points of the second-order λ transition, because for the tricritical phenomena the upper critical dimension is $d^* = 3$, whereas for the critical ones it is $d^* = 4$. The critical phenomena near the λ transition of ^{4}He have been studied using renormalization group theory [34].

Our paper is organized as follows. In Sec. II we introduce the model, and in Sec. II A we carry out a mean field approximation to it. In Sec. II B we discuss a procedure for finding that range of values of interaction constants of the model for which it exhibits a phase diagram similar to that of actual ^{3}He-^{4}He mixtures. We continue in Sec. III with studying the wetting films for short-ranged surface fields. Next, we calculate TCFs and their scaling functions and compare our results with those for the slab geometry by applying a suitable slab approximation to the present case. In Sec. IV we conclude with a summary. Appendix A contains important technical details.

II. THE MODEL

In order to model ^{3}He-^{4}He mixtures in the presence of a solid, two-dimensional surface, we consider a three-dimensional ($d = 3$) simple cubic lattice formed by L layers of two-dimensional $N \times N$ lattices with lattice spacing a. In the following all lengths are measured in units of a, which is equivalent to consider these lengths to be dimensionless together with setting $a = 1$. In each layer, all $\mathcal{N} := N^2$ lattice sites are identical. The different lattice sites are label by $\{i \mid i = 1,\dots,L\mathcal{N}\}$. Alternatively, one can use the index l, labeling the layer number, and the index v_l, referring to lattice sites within the lth layer. The lattice sites $\{i \mid i = 1,\dots,L\mathcal{N}\} = \{(l,v_l) \mid l = 0,\dots,L-1; v_l = 1,\dots,\mathcal{N}\}$ are occupied by either ^{3}He or ^{4}He atoms, or they are unoccupied. We consider nearest-neighbor interactions with the Hamiltonian

$$\mathcal{H} = -J_{44}N_{44} - J_{33}N_{33} - J_{34}N_{34} - [\mu_4 + f_4(l)]N_4 - [\mu_3 + f_3(l)]N_3 - J_s\tilde{N}_{44}, \qquad (1)$$

where N_{mn}, with m,n ∈ {3,4}, denotes the number of pairs of nearest neighbors of species $^{\mathrm{m}}$He and $^{\mathrm{n}}$He on the lattice sites. N_{m} denotes the number of $^{\mathrm{m}}$He atoms and $-J_s\tilde{N}_{44}$ is the sum of the interaction energies between the superfluid degrees of freedom Θ_i and Θ_j associated with the nearest-neighbor pairs $\langle i,j\rangle$ of ^{4}He with J_s as the corresponding interaction strength [see, cf., Eq. (4)]. The effective interactions between pairs of helium isotopes are represented by J_{33}, J_{44}, and J_{34}. The three effective pair potentials between the two types of isotopes are not identical due to their distinct statistics and the slight differences in their electronic states. The surface fields, which represent the effective interaction between the surface and the ^{4}He and ^{3}He atoms, are denoted as $f_4(l)$ and $f_3(l)$, respectively. In general these surface fields depend on the distance l from the surface, which is located at $l = 0$, and vanish for large l. The chemical potential of species $^{\mathrm{m}}$He is denoted as μ_{m}. [The Hamiltonian in Eq. (1) with $J_s = 0$ describes a classical binary liquid mixture of species m and n.]

In order to proceed, we associate an occupation variable s_i with each lattice site $\{i\}$, which can take the three values $+1$, -1, or 0, where $+1$ denotes that the lattice site is occupied by ^{4}He, -1 denotes that the lattice site is occupied by ^{3}He, and 0 denotes that the lattice site is unoccupied.

N_{m} and N_{mn} can be expressed in terms of $\{s_i\}$ as follows:

$$\begin{aligned}
N_4 &= \frac{1}{2}\sum_i s_i(s_i+1) \equiv \sum_i p_i,\\
N_3 &= \frac{1}{2}\sum_i s_i(s_i-1),\\
N_{44} &= \frac{1}{4}\sum_{\langle i,j\rangle}[s_i(s_i+1)s_j(s_j+1)] \equiv \sum_{\langle i,j\rangle} p_i p_j,\\
N_{33} &= \frac{1}{4}\sum_{\langle i,j\rangle}[s_i(s_i-1)s_j(s_j-1)],\\
N_{34} &= \frac{1}{4}\sum_{\langle i,j\rangle}[s_i(s_i+1)s_j(s_j-1) + s_i(s_i-1)s_j(s_j+1)],
\end{aligned} \qquad (2)$$

where $\sum_{\langle i,j\rangle}$ denotes the sum over nearest neighbors. Using the above definitions one obtains

$$\begin{aligned}\mathcal{H} = &-K\sum_{\langle i,j\rangle} s_i s_j - J\sum_{\langle i,j\rangle} q_i q_j - C\sum_{\langle i,j\rangle}(s_i q_j + q_i s_j)\\ &- \mu_-\sum_i s_i - \mu_+\sum_i q_i - \sum_i f_-(l) s_i - \sum_i f_+(l) q_i\\ &- J_s\sum_{\langle i,j\rangle} p_i p_j \cos(\Theta_i - \Theta_j),\end{aligned} \tag{3}$$

where

$$\begin{aligned}&\sum_{\langle i,j\rangle} p_i p_j \cos(\Theta_i - \Theta_j)\\ &\quad = \tilde{N}_{44} = \sum_{\langle i,j\rangle} p_i p_j \begin{pmatrix}\cos\Theta_i\\ \sin\Theta_i\end{pmatrix}\cdot\begin{pmatrix}\cos\Theta_j\\ \sin\Theta_j\end{pmatrix}\end{aligned} \tag{4}$$

and

$$\begin{aligned}q_i &= s_i^2,\\ p_i &= \tfrac{1}{2}s_i(s_i+1),\\ K &= \tfrac{1}{4}(J_{44}+J_{33}-2J_{34}),\\ J &= \tfrac{1}{4}(J_{44}+J_{33}+2J_{34}),\\ C &= \tfrac{1}{4}(J_{44}-J_{33}),\\ \mu_- &= \tfrac{1}{2}(\mu_4-\mu_3),\\ \mu_+ &= \tfrac{1}{2}(\mu_4+\mu_3),\\ f_+(l) &= \tfrac{1}{2}[f_4(l)+f_3(l)],\\ f_-(l) &= \tfrac{1}{2}[f_4(l)-f_3(l)].\end{aligned} \tag{5}$$

$\Theta_i \in [0,2\pi]$ represents the superfluid degree of freedom at the lattice site i, provided it is occupied by ^{4}He.

A. Mean field approximation

In this section we carry out a mean field approximation for the present model (for details of the calculations see Appendix A). The symmetry of the problem implies that all statistical quantities exhibit the same mean values for all lattice sites within a layer, in particular the same mean field generated by their neighborhood. Therefore all quantities depend only on the distance l of a layer from the surface. (Note that l is an integer which not only represents the position of the layer but also marks the corresponding layer.) We define the following dimensionless OPs:

$$\begin{aligned}X_l &:= \langle s_{(l,v_l)}\rangle,\\ D_l &:= \langle q_{(l,v_l)}\rangle,\\ M_l^2 &:= \langle p_{(l,v_l)}\sin\Theta_{(l,v_l)}\rangle^2 + \langle p_{(l,v_l)}\cos\Theta_{(l,v_l)}\rangle^2,\end{aligned} \tag{6}$$

which are coupled by the following self-consistent equations:

$$X_l = \frac{-W_l + R_l I_0(\beta J_s \tilde{M}_l)}{1 + W_l + R_l I_0(\beta J_s \tilde{M}_l)}, \tag{7}$$

$$D_l = \frac{W_l + R_l I_0(\beta J_s \tilde{M}_l)}{1 + W_l + R_l I_0(\beta J_s \tilde{M}_l)}, \tag{8}$$

and

$$M_l = \frac{R_l I_1(\beta J_s \tilde{M}_l)}{1 + W_l + R_l I_0(\beta J_s \tilde{M}_l)}, \tag{9}$$

where $\beta = 1/T$ with T as temperature times k_B, $I_0(\beta J_s \tilde{M}_l)$ and $I_1(\beta J_s \tilde{M}_l)$ are modified Bessel functions, and

$$\tilde{M}_l = (1-\delta_{l,0})M_{l-1} + 4M_l + M_{l+1}. \tag{10}$$

The dimensionless functions W_l and R_l depend on the following set of parameters:
$(X_l, D_l; \mu_-, \mu_+, f_+(l), f_-(l), T)$. They are given by

$$\begin{aligned}&W_l(X_l,D_l;\mu_-,\mu_+,f_+(l),f_-(l),T)\\ &\quad = \exp(\beta\{(J-C)[D_{l-1}(1-\delta_{l,0}) + 4D_l + D_{l+1}]\\ &\qquad + (C-K)[X_{l-1}(1-\delta_{l,0}) + 4X_l + X_{l+1}]\\ &\qquad + \mu_+ + f_+(l) - \mu_- - f_-(l)\})\end{aligned} \tag{11}$$

and

$$\begin{aligned}&R_l(X_l,D_l;\mu_-,\mu_+,f_+(l),f_-(l),T)\\ &\quad = \exp(\beta\{(J+C)[D_{l-1}(1-\delta_{l,0}) + 4D_l + D_{l+1}]\\ &\qquad + (C+K)[X_{l-1}(1-\delta_{l,0}) + 4X_l + X_{l+1}]\\ &\qquad + \mu_+ + f_+(l) + \mu_- + f_-(l)\}).\end{aligned} \tag{12}$$

Accordingly, the equilibrium free energy per number of lattice sites in a single layer is given by

$$\begin{aligned}\phi/\mathcal{N} = \sum_{l=0}^{L-1}\Bigg(&\frac{K}{2}X_l[4X_l + X_{l+1} + X_{l-1}(1-\delta_{l,0})]\\ &+ \frac{J}{2}D_l[4D_l + D_{l+1} + D_{l-1}(1-\delta_{l,0})]\\ &+ \frac{C}{2}X_l[4D_l + D_{l+1} + D_{l-1}(1-\delta_{l,0})]\\ &+ \frac{C}{2}D_l[4X_l + X_{l+1} + X_{l-1}(1-\delta_{l,0})]\\ &+ \frac{J_s}{2}M_l[4M_l + M_{l+1} + M_{l-1}(1-\delta_{l,0})]\\ &+ (1/\beta)\ln(1-D_l)\Bigg).\end{aligned} \tag{13}$$

Within the grand-canonical ensemble the pressure is $P = -\phi/V$, where here the volume is $V = L\mathcal{N}a$, with $a = 1$. The functional form of the expressions for the chemical potentials are obtained by solving Eqs. (7) and (8) for them (see Appendix A):

$$\begin{aligned}\mu_+ = &\frac{T}{2}\ln\left(D_l^2 - X_l^2\right) - T\ln 2 - T\ln(1-D_l)\\ &- \frac{T}{2}\ln[I_0(\beta J_s \tilde{M}_l)] - J[D_{l-1}(1-\delta_{l,0}) + 4D_l + D_{l+1}]\\ &- C[X_{l-1}(1-\delta_{l,0}) + 4X_l + X_{l+1}] - f_+(l)\end{aligned} \tag{14}$$

and

$$\begin{aligned}\mu_- = &\frac{T}{2}\ln\frac{D_l + X_l}{D_l - X_l} - \frac{T}{2}\ln[I_0(\beta J_s \tilde{M}_l)]\\ &- C[D_{l-1}(1-\delta_{l,0}) + 4D_l + D_{l+1}]\\ &- K[X_{l-1}(1-\delta_{l,0}) + 4X_l + X_{l+1}] - f_-(l).\end{aligned} \tag{15}$$

Finally, one can express the magnetization M_l in terms of X_l and D_l by using Eqs. (7)–(9):

$$\frac{X_l + D_l}{2} = \frac{M_l I_0(\beta J_s \tilde{M}_l)}{I_1(\beta J_s \tilde{M}_l)}. \tag{16}$$

According to the definition of the OPs in Eq. (6) and by using Eqs. (2) and (A7) one can express the number densities of species ^{4}He and ^{3}He in the lth layer as

$$\begin{aligned} X_{4,l} &= \frac{\langle N_{4,l}\rangle}{\mathcal{N}} = \langle p_l\rangle = \frac{1}{2}\langle s_l(s_l+1)\rangle = \frac{D_l + X_l}{2}, \\ X_{3,l} &= \frac{\langle N_{3,l}\rangle}{\mathcal{N}} = \frac{1}{2}\langle s_l(s_l-1)\rangle = \frac{D_l - X_l}{2}, \end{aligned} \tag{17}$$

so that $D_l = X_{4,l} + X_{3,l} = \langle s_l^2\rangle$ and $X_l = X_{4,l} - X_{3,l} = \langle s_l\rangle$, where $s_l \equiv s_{(l,v_l)}$ is the occupation variable of a single lattice site within the lth layer; its thermal average is independent of v_l (see Appendix A). Accordingly, the concentration of the two species in the lth layer is given by $\mathcal{C}_{4,l} \equiv \frac{X_{4,l}}{X_{4,l}+X_{3,l}} = \frac{D_l+X_l}{2D_l}$ and $\mathcal{C}_{3,l} \equiv \frac{X_{3,l}}{X_{4,l}+X_{3,l}} = \frac{D_l-X_l}{2D_l}$.

In order to study wetting films at given values of (T,μ_+,μ_-), one has to solve the set of equations given by Eqs. (14)–(16) for the set of OPs $\{(X_l,D_l,M_l)\,|\,l=0,\ldots,L-1\}$. Since Eqs. (7)–(9) cannot be solved analytically, we did so numerically by using the GSL library [35]. Since for the last layer $l=L-1$ Eqs. (14) to (16) request OP values at $l=L$, one has to assign values to (X_L,D_L,M_L). If the system size L is sufficiently large one expects that far away from the surface the OP profiles attain their bulk values. This implies $(X_L,D_L,M_L) = (X_{\text{bulk}},D_{\text{bulk}},M_{\text{bulk}})$. The system size L can be considered to be large enough if the OP profiles (X_l,D_l,M_l) remain *de facto* unchanged upon increasing L (which mimics a semi-infinite system). The minimization procedure, which leads to Eqs. (14)–(16), does not involve the second derivative of ϕ with respect to the trial density matrix ρ_l (see Appendix A). Therefore, depending on the initial profile $\{(X_l,D_l,M_l)\,|\,l=0,\ldots,L-1\}$, with which one starts the iteration algorithm, the solution of Eqs. (14)–(16) might correspond to a local minimum, a local maximum, or a saddle point.

B. Bulk phase diagram

Since the realization of the experimental paths in Ref. [3] requires the knowledge of the bulk phase diagram, first one has to find the set of coupling constants, for which the model exhibits a phase diagram similar to that of actual ^{3}He-^{4}He mixtures. Taking the OPs to be independent of l and omitting the surface fields, i.e., $f_+(l) = f_-(l) = 0$, Eqs. (7)–(9), and Eqs. (14)–(16), together with the expression for the equilibrium free energy given by Eq. (13), render the bulk phase diagram of the system as studied in Ref. [33]. It has been demonstrated in Ref. [33] (see also Refs. [36] and [37]) that various coupling constants lead to diverse topologies of the phase diagram for the bulk liquid-liquid demixing transitions. The topologies discussed in Ref. [33] range from the phase diagram of a classical binary mixture [Figs. 4(a) and 5] to a phase diagram which to a large extent resembles the actual one of ^{3}He-^{4}He mixtures [Fig. 4(b)]. In Sec. III A we consider a classical binary liquid mixture with the bulk phase diagram as in Fig. 4(a). However, when studying wetting films of ^{3}He-^{4}He

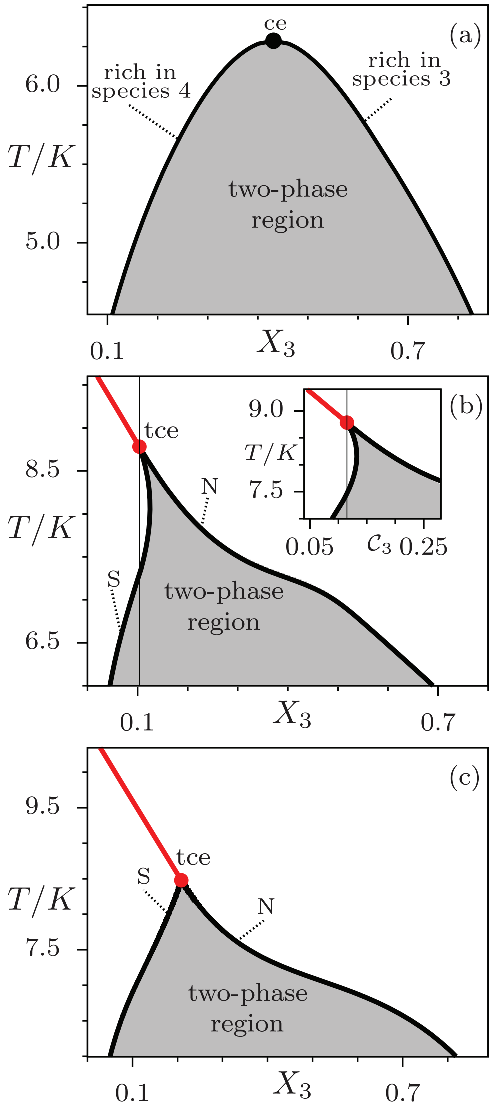

FIG. 4. Liquid-liquid demixing phase transitions in the bulk at coexistence with the vapor phase (the vapor phase is not shown here) in the (X_3, T) plane, with $X_3 = \langle N_3\rangle/(L\mathcal{N}) = D - X$ for (a) $(C/K, J/K, J_s/K) = (1,5.714,0)$, (b) $(C/K, J/K, J_s/K) = (1,5.714,3.674)$, and (c) $(C/K, J/K, J_s/K) = (1,9.107,3.701)$. The inset of panel (b) shows the same phase diagram in the $(T,\mathcal{C}_3)$ plane, where $\mathcal{C}_3 = X_3/D$ denotes the concentration of ^{3}He. The phase diagrams in (a) and (b) have been discussed in detail in Ref. [33]. (Note that in Ref. [33] the coupling constants are rescaled by a factor of 6 and the total number of lattice sites are denoted as $\mathcal{N}$, whereas here the total number of lattice sites is given by $L\mathcal{N}$.) In (b) and (c) the black curves denote the binodals of the first-order phase transitions between the normal fluid (N) and the superfluid (S). The lines of first-order phase transitions in (a) terminate at the critical end point ce with $T_{\text{ce}}/K = 6.286$, whereas in (b) and (c) the lines of first-order phase transitions terminate at a tricritical end point tce. In (b) and (c) the red curve denotes the λ line of second-order phase transitions between the normal fluid and the superfluid. The temperature of the tricritical end point in panels (b) and (c) are $T_{\text{tce}}/K = 8.782$ and $T_{\text{tce}}/K = 8.47974$, respectively. In (b) the thin vertical line indicates $X_3 = X_3^{\text{tce}}$, whereas in the inset of this figure the thin vertical line indicates $\mathcal{C}_3 = \mathcal{C}_3^{\text{tce}}$. The short dotted strokes indicate the character (S, N, rich in species 4, or rich in species 3) of the corresponding binodal. (See also Appendix B.)

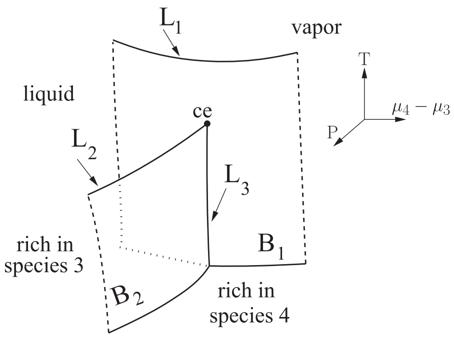

FIG. 5. Fluid parts of the phase diagram of a classical binary liquid mixture in the $(T,P,\mu_4-\mu_3)$ space (schematic diagram). B$_1$ is the surface of first-order liquid-vapor phase transitions, whereas B$_2$ is the surface of first-order liquid-liquid demixing transitions, between phases rich in either species 3 or 4. The surface B$_1$ terminates at a line L$_1$ of critical points. L$_2$ denotes the line of critical points of the liquid-liquid demixing transitions, which ends at the surface B$_1$ at the critical end point ce. The surfaces B$_1$ and B$_2$ intersect along a line L$_3$ of triple points. The dashed curves indicate that the corresponding surfaces continue. The demixing two-phase region in terms of temperature and the number density X_3 of species 3 for the liquid phases coexisting along L$_3$ are shown in Fig. 4(a); the vapor phase is not shown there.

mixtures in Sec. III B, instead of the phase diagram in Fig. 4(b) we consider the one in Fig. 4(c). The reason for this choice is discussed in Appendix B.

III. LAYERING AND WETTING FOR SHORT-RANGED SURFACE FIELDS

In this section we study the layering and wetting behavior [38] of the present model with short-ranged surface fields $f_+(l)=\tilde{f}_+\delta_{l,0}$ and $f_-(l)=\tilde{f}_-\delta_{l,0}$. The field $f_+(l)$ describes the enhancement of the fluid density near the wall, whereas $f_-(l)$ expresses the preference of the wall for ^{4}He over ^{3}He.

Within the present model μ_+ is the field conjugate to the number density order parameter D_l. By changing μ_+ from its value $\mu_+^{\mathrm{co}}(P,T)$ at liquid-vapor coexistence and at a given temperature T and pressure P, one can drive the bulk system either towards the liquid phase ($\Delta\mu_+=\mu_+-\mu_+^{\mathrm{co}}>0$) or towards the vapor phase ($\Delta\mu_+<0$). In order to realize the experimental conditions we choose $\Delta\mu_+<0$ such that the bulk system remains thermodynamically in the vapor phase. With this constraint we determine the solution of Eqs. (14)–(16) for set of the OPs $\{(X_l,D_l,M_l)\,|\,l=0,\ldots,L-1\}$. We find that the occurrence of wetting films as well as their thicknesses depend on the strength of the surface fields $\tilde{f}_+$ and $\tilde{f}_-$. Since along the experimental paths taken in Ref. [3] the system is in the complete wetting regime, we choose such values of the surface fields for which complete wetting does occur. We refrain from exploring the full variety of scenarios for wetting transitions which can occur within the present model.

Based on the number density profile D_l one can define the film thickness as [38]

$$y(\mu_-,\mu_+,\tilde{f}_+,\tilde{f}_-,T)=\frac{\varrho}{D_{\mathrm{m}}-D_{\mathrm{b}}}, \tag{18}$$

where D_b is the bulk density of the vapor phase,

$$\varrho=\sum_{l=0}^{L-1}(D_l-D_{\mathrm{b}}) \tag{19}$$

is the excess adsorption, and D_{m} is the density of the metastable liquid phase at the thermodynamic state corresponding to the stable vapor phase. Alternatively, one can define y as the position of the inflection point of the density profile D_l at the emerging liquid-vapor interface. In Figs. 8, 9, and 15–17 y is calculated via Eq. (18), whereas in Fig. 11 as an example we have calculated y via the inflection point of the density profile. The profile $X_l=X_{4,l}-X_{3,l}$ indicates, whether the various layers are occupied mostly by species of type 4 (positive or large values of X_l) or by species of type 3 (negative or small values of X_l). A nonzero magnetization profile signals that the wetting film is superfluid. In the following subsections we present our results for $J_s=0$ (Sec. III A), which corresponds to a classical binary mixture, and $J_s\neq 0$ (Sec. III B), which corresponds to a ^{3}He-^{4}He mixture. The former case shows how within the present model the strength of the surface fields influences the formation and the thickness of the wetting films, whereas the latter case focuses on describing the present, experimentally relevant situation.

A. Layering and wetting for $J_s=0$

In this subsection we consider a classical binary liquid mixture of species 3 and 4, described by the Hamiltonian given in Eq. (3) with the coupling constants $(C/K,J/K,J_s/K)=(1,5.714,0)$. The bulk phase diagram of this system in the (T,X_3) plane is shown in Fig. 4(a). All figures in this subsection (i.e., Figs. 6–10) share the coupling constants $(C/K,J/K,J_s/K)=(1,5.714,0)$. In Figs. 6(a) and 7–10 the system size is $L=40$, whereas in Fig. 6(b) it is $L=80$. We study how the strengths of the surface fields influence the formation of the wetting films for thermodynamic states with $T>T_{\mathrm{ce}}$ and $\Delta\mu_+=\mu_+-\mu_+^{\mathrm{co}}<0$, i.e., corresponding to the vapor being the bulk phase and the wetting phase being the mixed supercritical liquid phase.

We start our discussion by taking $\tilde{f}_-=0$ and varying $\tilde{f}_+$. We find that weak surface fields $\tilde{f}_+$ cannot stabilize high-density layers near the surface, so that the model does not exhibit wetting by the mixed-liquid phase. Instead, for weak $\tilde{f}_+$ the wall prefers the vapor phase so that upon approaching the liquid-vapor coexistence from the liquid side (i.e., $\Delta\mu_+\to 0^+$) a vapor film forms close to the wall corresponding to drying of the interface between the wall and the mixed liquid.

Covering the case of weak surface fields, Fig. 6(a) shows the number density profiles for $(\tilde{f}_+,\tilde{f}_-)/K=(0.857,0)$ at $\Delta\mu_+/K=(\mu_+-\mu_+^{\mathrm{co}})/K=-8.57\times10^{-4}$, i.e., on the vapor side for several temperatures above T_{ce} and at fixed $X_3=X_3^{\mathrm{ce}}$. Figure 6(b) shows the number density profiles for the same bulk system with the same surface fields but for $\Delta\mu_+/K=(\mu_+-\mu_+^{\mathrm{co}})/K=+8.57\times10^{-4}$ so that the stable bulk phase is liquid. Since the wall prefers the vapor phase, upon increasing T a drying film forms at the surface of the solid substrate.

For larger values of $\tilde{f}_+$ (see Fig. 7), i.e., for $(\tilde{f}_+,\tilde{f}_-)/K=(5.143,0)$, at lower temperatures T we find monotonically decaying density profiles without shoulder formation, whereas

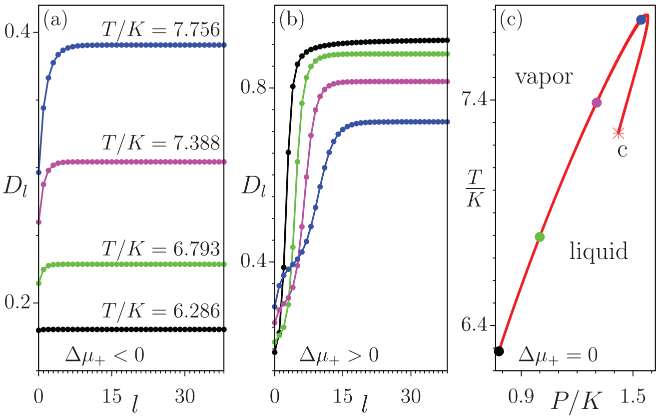

FIG. 6. Number density profiles for weak surface fields $(\tilde{f}_+,\tilde{f}_-)/K = (0.857,0)$ and for several values of temperature T (same color code in all panels) above $T_{\mathrm{ce}}/K = 6.286$ and at $X_3 = X_3^{\mathrm{ce}} = 0.431$ in the liquid phase, with (a) $\Delta\mu_+/K = -8.57\times10^{-4}$ and (b) $\Delta\mu_+/K = +8.57\times10^{-4}$. In (a) the bulk phase is the vapor phase, whereas in (b) it is the coexisting liquid phase with slight offsets. Panel (c) shows the liquid-vapor coexistence line (red curve) in the (P,T) plane, emerging under the constraint $X_3 = X_3^{\mathrm{ce}}$ in the liquid phase. The colored dots in panel (c) indicate the thermodynamic states with the same temperature values as in panels (a) and (b), which, unlike in these two panels, lie at liquid-vapor coexistence. The star denotes the liquid-vapor critical point $(P_{\mathrm{c}}/K,T_{\mathrm{c}}/K) = (1.422,7.230)$. The thermodynamic paths in panels (a) and (b) follow the red curve in panel (c) but with the corresponding offset values $\Delta\mu_+$. In panel (a) the corresponding thermodynamic states are: $(T/K,D = X_4 + X_3,X = X_4 - X_3,M) = \{(6.286,0.181,-0.121,0),(6.793,0.229,-0.137,0),(7.388,0.304,-0.155,0),(7.756,0.391,-0.174,0)\}$. The vapor bulk phase in (a) is preferred by the wall. Accordingly, there are no liquidlike wetting films. In panel (a) near T_{c} critical adsorption (see Fig. 8 in Ref. [39]) of the preferred vapor phase occurs, which is indicated by the increased depth and range of the minimum in D_l. In panel (b), due to $\Delta\mu_+ > 0$ the stable bulk phase is the liquid. Since the vapor phase is preferred by the wall drying films form there upon increasing the temperature. The corresponding thermodynamic states are $(T/K,D,X,M) = \{(6.286,0.913,0.050,0), (6.793,0.878, 0.015,0),(7.388,0.815, -0.048,0), (7.756,0.722, -0.141,0)\}$. The value of μ_- can be obtained from Eq. (15) using the values of (T,D,X,M) for the corresponding thermodynamic states as provided above. Note that the nonmonotonic behavior of the red curve in (c) is caused by the constraint $X_3 = X_3^{\mathrm{ce}}$. For (c), in order to identify the vapor and liquid phases, in addition to T and P also the value of the chemical potential μ_- is required, which is not shown.

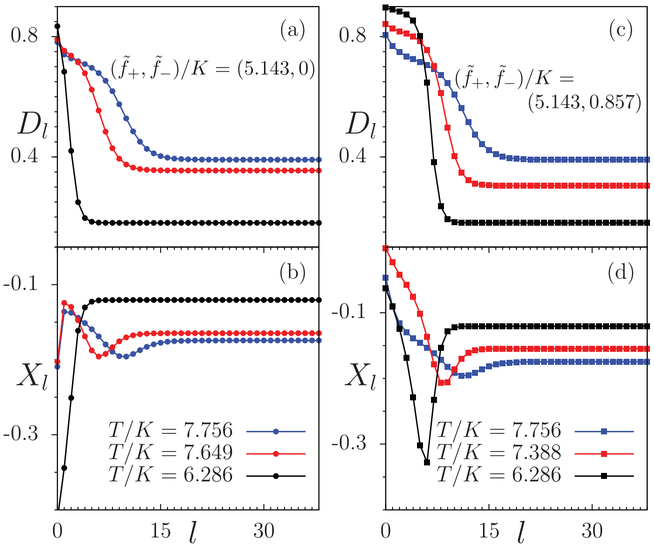

FIG. 7. Order parameter profiles D_l and X_l at $X_3 = X_3^{\mathrm{ce}} = 0.431$ and for $\Delta\mu_+/K = -8.57\times10^{-4}$ for several temperatures and for two sets of surfaces fields. In panels (a) and (b) the surface fields are $(\tilde{f}_+,\tilde{f}_-)/K = (5.143,0)$, whereas panels (c) and (d) correspond to $(\tilde{f}_+,\tilde{f}_-)/K = (5.143,0.857)$. The bulk phase is the vapor phase and the wall prefers the liquid phase, giving rise to wetting films. The positive value of $\tilde{f}_-$ not only results in the increase of the number density $X_{4,l}$ of species 4 and hence also of X_l in the first layer [see panel (d)], but also increases the total number density D_l in the first layer [see panel (c)]. The stable thermodynamic states of the vapor phase in the bulk are $(T/K,D,X,M) = \{(6.286,0.180,-0.121,0),\ (7.388,0.304,-0.155,0),\ (7.649,0.355, -0.165,0),(7.756,0.391,-0.174,0)\}$. All three bulk states lie in the vapor phase close to liquid-vapor coexistence on the left side of the red line shown Fig. 6(c). The value of μ_- can be obtained from Eq. (15) using the values of (T,D,X,M) for the corresponding thermodynamic states as provided above.

at higher temperatures the density profiles tend to exhibit plateaus characteristic of wetting [see Fig. 7(a)]. Note that in Figs. 7(a) and 7(b) the number density in the first layer as part of the wetting film decreases upon increasing T. This is in accordance with the fact that the density of the bulk liquid phase as the wetting phase decreases upon heating, whereas the bulk vapor density increases. The profiles $X_l = X_{4,l} - X_{3,l}$ shown in red and blue in Fig. 7(b) have local minima at $l = 5$ and $l = 9$, respectively. These minima occur approximately at the position of the emerging liquid-vapor interface [see the corresponding curves in panel (a)] and indicate that species of type 3 preferentially accumulate at the liquid-vapor interface.

Figures 7(c) and 7(d) show the OP profiles for $(\tilde{f}_+,\tilde{f}_-)/K = (5.143,0.857)$ and $\Delta\mu_+/K = -8.57\times10^{-4}$ at several values of the temperature. One can see that for positive values of $\tilde{f}_-$ both D_l and X_l are enhanced in the first layer. This corresponds to the preferential adsorption of species of type 4 at the wall.

In order to see how the wetting films grow upon approaching the liquid-vapor coexistence surface, we fix T and vary $\Delta\mu_+$. Figure 8 shows the film thickness y/a versus $\Delta\mu_+$ for $(\tilde{f}_+,\tilde{f}_-)/K = (8.571,0)$ and for several temperatures; y is calculated according to Eq. (18). For low temperatures, upon approaching the liquid-vapor coexistence surface the film thickness increases smoothly and reaches a plateau. This corresponds to incomplete wetting. The height of this plateau increases gradually upon increasing T towards $7.097 < T_w/K < 7.123$, which corresponds to a critical wetting transition between incomplete and complete wetting [38]. The corresponding line of wetting transitions lies on the surface of the liquid-vapor transitions (B_1 in Fig. 5) between the critical end point ce and and the line of critical points of the liquid-vapor transitions (L_1 in Fig. 5). Note that Fig. 8 provides a semilogarithmic plot so that the linear growth of the film thickness on this scale confirms the theoretically expected logarithmic growth of the film thickness $y \sim \log(|\Delta\mu_+|/K)$

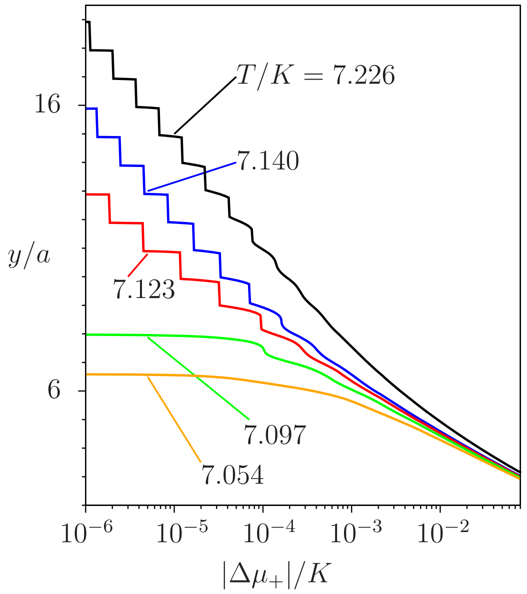

FIG. 8. Film thickness y/a versus $|\Delta\mu_+|/K$ for $(\tilde{f}_+,\tilde{f}_-)/K = (8.571{,}0)$ at $X_3 = X_3^{\rm ce}$ and for several temperatures. Upon approaching the liquid-vapor coexistence surface at low temperatures, the film thickness increases smoothly and reaches a plateau. The height of this plateau increases gradually by increasing T, indicating $7.097 < T_w/K < 7.123$. The jumps are due to first-order layering transitions induced by the lattice model. Above the roughening transition they are an artifact of mean field theory [38]. For $T > T_w$ one has $y(\Delta\mu_+ \to 0^-) \sim \kappa \ln \frac{1}{|\Delta\mu_+|/K}$ with a slight increase of $\kappa(T)$ as a function of T.

for short-ranged surface fields [38]. At higher temperatures T the film thickness does not increase smoothly anymore but exhibits jumps due to layering transition. Figure 9 shows the location of these layering transitions in the (μ_+,T) plane for $(\tilde{f}_+,\tilde{f}_-)/K = (8.571{,}0)$. If a thermodynamic path passes through any of these lines, the film thickness undergoes a small jump of the size $l \simeq 1$. Each line of the layering transitions ends at a critical point. Along thermodynamic paths, which pass by these critical points the jumps of the film thickness become rounded as for the green and red curves in Fig. 8. The color code in Fig. 9 does not carry a particular meaning; the lines are colored differently so that it is easier to distinguish them. The closer the system is to the liquid-vapor coexistence surface, i.e., the smaller $|\Delta\mu_+|$ is, the closer are the lines of layering transitions. Figure 10 shows how the increasing density of the layering transition lines affects the film thickness while varying the temperature at fixed values of $\Delta\mu_+/K = -8.57\times10^{-8}$ and $X_3 = X_3^{\rm ce} = 0.431$.

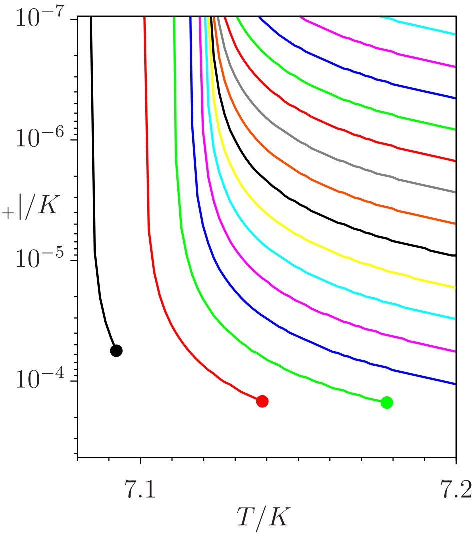

FIG. 9. Layering transitions in the (μ_+,T) plane for $(\tilde{f}_+,\tilde{f}_-)/K = (8.571{,}0)$. Each line of first-order layering transition ends at a critical point. The color code does not carry a specific meaning. The lines are colored differently so that it is easier to distinguish them.

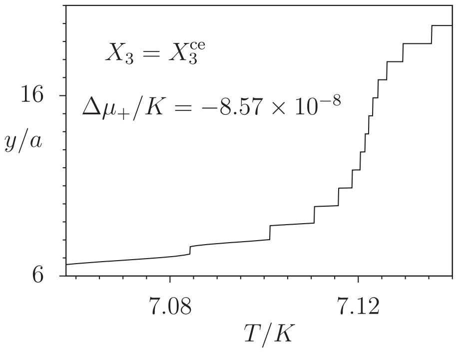

FIG. 10. Equilibrium film thickness y/a as a function of temperature for $\Delta\mu_+/K = -8.57\times10^{-8}$ and $X_3 = X_3^{\rm ce}$. Since $\Delta\mu_+$ is nonzero, $y(T)$ does not diverge but attains a maximum upon passing by T_w. This maximum diverges for $\Delta\mu_+ \to 0$. The jumps are bunched together around $T/K \simeq 7.125$ and spread-out otherwise.

B. Layering and wetting for $J_s \neq 0$

In order to describe wetting films of ^{3}He-^{4}He mixtures, we focus on systems exhibiting phase diagrams with nonzero values of J_s as in Fig. 4(c), and we choose the surface fields $(\tilde{f}_+,\tilde{f}_-)/K = (10.714{,}16.071)$. All figures in this subsection (i.e., Figs. 11–17) share the coupling constants $(C/K,J/K,J_s/K) = (1{,}9.10714{,}3.70107)$, the surface fields $(\tilde{f}_+,\tilde{f}_-)/K = (10.714{,}16.071)$, and the system size $L = 60$. The growth of wetting films upon approaching the liquid-vapor coexistence surface is illustrated in Fig. 11. For all temperatures considered, upon approaching liquid-vapor coexistence the wetting films become thicker: $y(\Delta\mu_+ \to 0^-) \sim \kappa \ln \frac{1}{|\Delta\mu_+|/K}$ with a significant temperature dependence of the amplitude κ. This is different from the situation in Fig. 8 with $J_s = 0$, where only for sufficiently high temperatures (i.e., $T > T_w$) complete wetting occurs. This means that in Fig. 11T_w is below the considered temperature interval. Interestingly, in Fig. 11 at the reduced temperature $(T - T_{\rm tce})/T_{\rm tce} \approx -0.016$ the film thickness exhibits the most rapid increase upon approaching the liquid-vapor coexistence surface (see the red curve), whereas for higher and lower temperatures the growth of the film thickness is reduced, i.e., the amplitude $\kappa(T)$ introduced above has a maximum at $(T - T_{\rm tce})/T_{\rm tce} \approx -0.016$. This is different from what one observes in Fig. 8, where the thickness of the wetting film is, via $\kappa(T)$, a

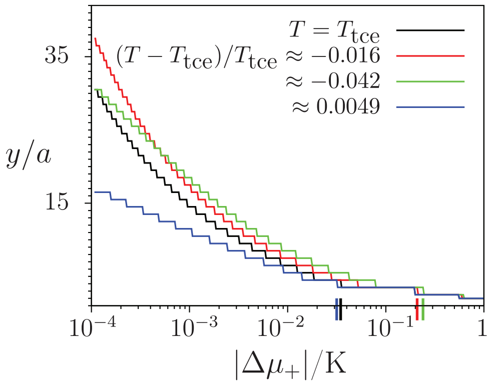

FIG. 11. Equilibrium film thickness y/a versus $|\Delta\mu_+|/K$ for $(\tilde{f}_+,\tilde{f}_-)/K = (10.714,16.071)$ and for four temperatures. Unlike the situation in Fig. 8 with $J_s = 0$, the thickness of the wetting films as a function of $|\Delta\mu_+|$ is a nonmonotonic function of T. The most rapid increase occurs at $(T - T_{\rm tce})/T_{\rm tce} \approx -0.016$, whereas for lower and higher temperatures the growth of the wetting film as a function of $\Delta\mu_+$ is slower. Upon approaching the liquid-vapor coexistence surface, the ^{4}He-rich layers within the wetting films become superfluid. At each temperature, the continuous surface transition to superfluidity occurs for values of the offset $|\Delta\mu_+|$ smaller than the one indicated by the corresponding tick on the abscissa with the same color. For $(T - T_{\rm tce})/T_{\rm tce} = -0.016$ and $(T - T_{\rm tce})/T_{\rm tce} = -0.042$, the number density of ^{3}He on the superfluid branch of the binodal [Fig. 4(c)] is $X_3 = 0.201$ and $X_3 = 0.188$, respectively, whereas for $T \geqslant T_{\rm tce}$ the number density of ^{3}He is fixed at $X_3 = X_3^{\rm tce} = 0.20845$.

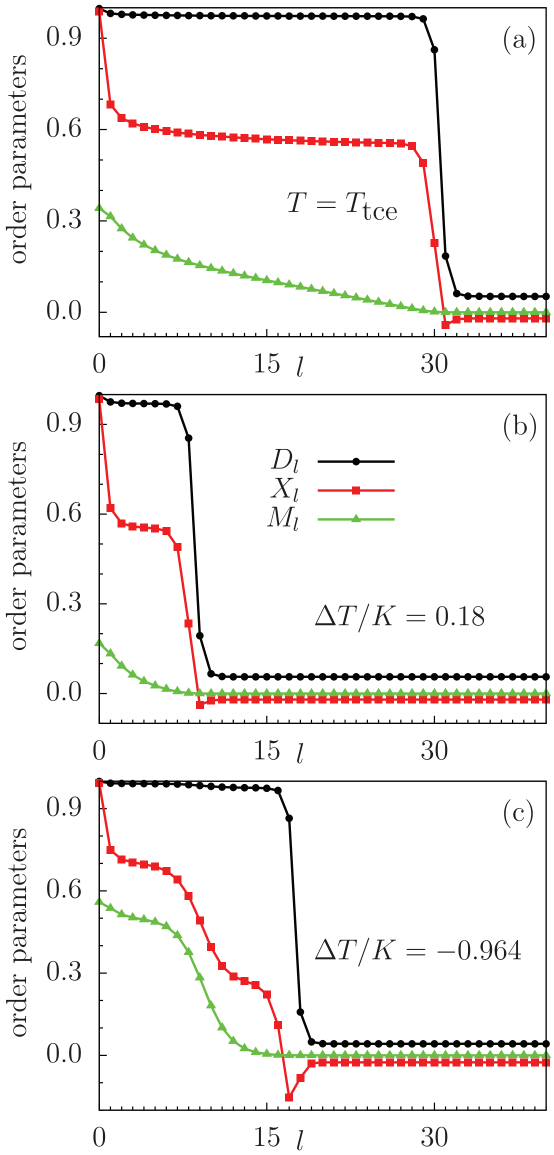

FIG. 12. Order parameter profiles D_l, X_l, and M_l for $(\tilde{f}_+,\tilde{f}_-)/K = (10.714,16.071)$ at $\Delta\mu_+/K = -1.07\times10^{-4}$ for the bulk states (a) $T = T_{\rm tce}$, $X_3 = X_3^{\rm tce}$, (b) $\Delta T/K = (T - T_{\rm tce})/K = 0.18$, $X_3 = X_3^{\rm tce}$, and (c) $\Delta T/K = (T - T_{\rm tce})/K = -0.964$, $X_3 = 0.1461$ (which is on the superfluid branch of the binodal [Fig. 4(c)]. For these bulk states, in panels (a)–(c) the stable vapor phase (i.e., $l \to \infty$) exhibits the order parameters $(D = X_4 + X_3, X = X_4 - X_3) = \{(0.0523,-0.0206),(0.0559,-0.0204),(0.0422,-0.0255)\}$, respectively ($M = 0$ for the vapor phase). The bulk parameters of the system are those for Fig. 4(c). The keys for the OP profiles are the same for all panels. The value of μ_- can be obtained from Eq. (15) using the values of (T,D,X,M) for the corresponding thermodynamic states as provided above.

monotonically increasing function of T. Note that in Fig. 11 for the curves with $T \geqslant T_{\rm tce}$ the number density of ^{3}He is fixed at $X_3 = X_3^{\rm tce} = 0.20845$. However, for $T < T_{\rm tce}$ the system phase separates and the number density of ^{3}He changes. Accordingly, in Fig. 11 for $(T - T_{\rm tce})/T_{\rm tce} = -0.016$ and $(T - T_{\rm tce})/T_{\rm tce} = -0.042$, the number density of ^{3}He on the superfluid branch of the binodal [Fig. 4(c)] is $X_3 = 0.201$ and $X_3 = 0.188$, respectively. The OP profiles for three temperatures at $\Delta\mu_+/K = -1.07\times10^{-4}$ are shown in Fig. 12. Due to the large value of $\tilde{f}_-$, the number density $X_{4,l}$ of ^{4}He is enhanced near the wall, and hence $X_l = X_{4,l} - X_{3,l}$ is large there. If the bulk liquid is in the normal fluid phase but close to either the λ line for $T > T_{\rm tce}$, or to the normal branch of the binodal [Fig. 4(c)] for $T < T_{\rm tce}$, this enhancement induces symmetry breaking of the superfluid OP near the wall. At the liquid-vapor coexistence surface, this so-called surface transition occurs at temperatures $T_s(X_3)$, which depend on the bulk number density X_3 of ^{3}He atoms or, equivalently, on the bulk concentration $\mathcal{C}_3$ of ^{3}He as $T_s(\mathcal{C}_3)$ (see Fig. 13). With the bulk being in the vapor phase, the continuous surface transition occurs within the wetting film for offsets $\Delta\mu_+$ from the liquid-vapor coexistence surface smaller than a certain temperature dependent value, which is marked in Fig. 11 by the tick along the abscissa colored accordingly. Upon crossing the continuous surface transition one observes a nonzero profile M_l in the wetting film [see Figs. 12(a) and 12(b)]. For $T < T_{\rm tce}$, for which the bulk liquid phase separates into a superfluid and a normal fluid phase, the OP profiles within the wetting films exhibit two plateaus, one corresponding to the superfluid phase [note the left plateau of M_l in Fig. 12(c)] and the other one (on the right side) corresponding to the normal fluid phase. The minimum of the profile X_l occurs at the emerging liquid-vapor interface at around (a) $l = 31$, (b) $l = 9$, and (c) $l = 17$. This demonstrates the effective attraction of ^{3}He towards the emerging liquid-vapor interface, which suppresses the superfluid OP at the liquid-vapor interface. On the other hand the preference of the wall for ^{4}He enhances the superfluid

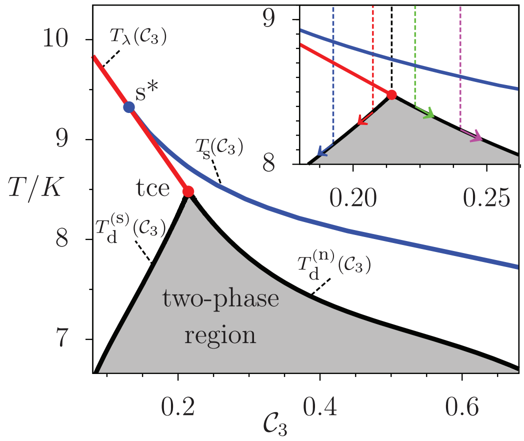

FIG. 13. The bulk liquid-liquid phase transitions at coexistence with the vapor phase as in Fig. 4(c) plotted in the $(T,\mathcal{C}_3)$ plane, with $\mathcal{C}_3 = (D - X)/(2D)$ as the concentration of ^{3}He (the vapor phase is not shown here). The blue line $T_s(\mathcal{C}_3)$ represents the continuous surface transition. Upon crossing this transition line a thin film near the wall becomes superfluid although the bulk remains a normal fluid. This line merges with the λ line [red line denoted as $T_\lambda(\mathcal{C}_3)$] at the special point s*. The inset shows the vertical thermodynamic paths (at liquid-vapor coexistence) taken experimentally. The numerical paths in our calculations are located in the vapor phase parallel to the ones in the inset. $T_d^{(s)}(\mathcal{C}_3)$ [$T_d^{(n)}(\mathcal{C}_3)$] denotes the superfluid [normal fluid] binodal of the two-phase region. The arrows indicate how the vertical thermodynamic paths continue after encountering the demixing curve. The path shown by the black dotted line can follow both binodals.

OP there as if there would be a surface field acting on the superfluid OP, which is, however, not the case.

The experimental data [3], reproduced in Fig. 14, have been obtained at liquid-vapor coexistence along the paths of fixed concentration $\mathcal{C}_3$ of ^{3}He as shown in the inset of Fig. 13 by the vertical dotted lines. [Note that in Fig. 14 X corresponds to the concentration of ^{3}He, which here is denoted by $\mathcal{C}_3 = (D - X)/(2D) = X_3/(X_3 + X_4)$. We have ignored the subscript l because we are referring to the bulk values.] The thermodynamic paths of fixed ^{3}He concentration followed in our calculations are parallel to the experimental ones but are located in the vapor phase close to the liquid-vapor coexistence surface (like the brown surface in Fig. 1).

The film thickness y/a versus temperature T along a path with an offset $\Delta\mu_+/K = -1.07\times10^{-4}$ parallel to the vertical black dashed line in Fig. 13 is shown in Fig. 15. Within the considered temperature range the system is above the wetting temperature T_w (not shown in the figure). We find that at fixed $\mathcal{C}_3$ the variation of the film thickness with temperature is nonmonotonic. Upon increasing the temperature, for $T > T_s$, the film thickness increases. A much steeper increase of the film thickness, associated with a break in slope, occurs between T_s and T_{tce}, where the TCFs emerge. (Note that due to the offset from liquid-vapor coexistence the sharp drop of y/a occurs slightly below T_{tce}; see Fig. 13.)

As discussed before, due to the surface transition close to T_{tce} the superfluid OP becomes nonzero near the wall. This profile vanishes at the emerging liquid-vapor interface, where the ^{3}He atoms accumulate. This behavior corresponds to the nonsymmetric, effective $(+,O)$ BCs for the superfluid order parameter M_l in the wetting film. Therefore, the resulting TCF acting on the liquid-vapor interface is repulsive and leads to an increase of the film thickness. The maximum film thickness occurs at $T_{peak}/K \approx 8.3346$, which lies below T_{tce}, in agreement with the experimental results (see Fig. 14) (T_{peak} is defined as the midpoint of the temperature range enclosing the maximum film thickness). T_s denotes the temperature of the surface transition. Figure 16 shows how the offset value $\Delta\mu_+$ affects the equilibrium film thickness y. As expected, upon increasing the offset value, the film thickness decreases. Moreover T_{peak} shifts towards lower temperatures.

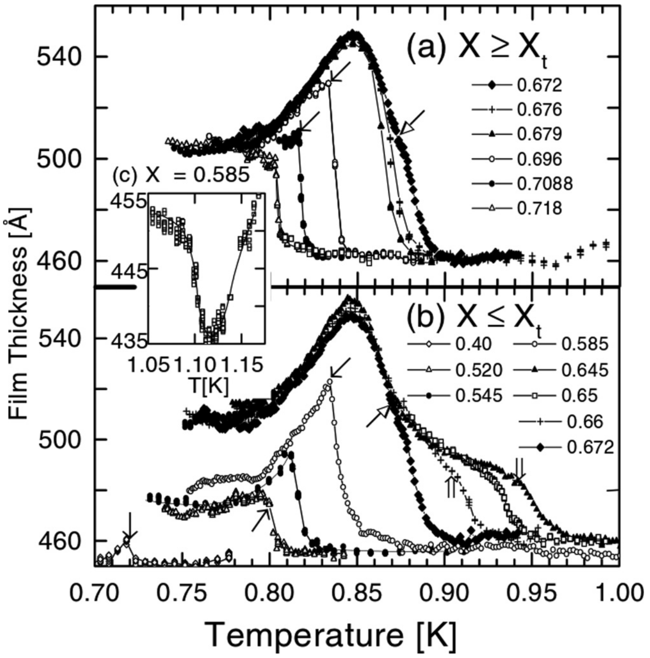

FIG. 14. Thickness of ^{3}He-^{4}He wetting films extracted from capacity measurements (Fig. 4 in Ref. [3]). The values of X refer to various concentrations of ^{3}He. The concentration of ^{3}He at the tricritical point is $X_t = 0.672$. Panels (a) and (b) correspond to $X \geqslant X_t$ and $X \leqslant X_t$, respectively. Thin arrows show the points, where the bulk liquid phase separates. The large headed arrow indicates the tricritical point. In (b) the arrows with double lines indicate the onset temperature of superfluidity. For the thermodynamic path on the superfluid side [panel (b)], the growth of the film thickness exhibits a characteristic shoulder between the tricritical temperature and the superfluid transition temperature on the λ line. The growth of the film thickness as a function of temperature is due to repulsive TCFs between the solid wall and the liquid-vapor interface, arising near the tricritical point. For small X the wetting film resembles a film of pure ^{4}He, which corresponds to (O,O) BCs for the CCFs arising near the temperature of the λ transitions, which are attractive [2] [see the dip in panel (c)]. This figure is, with permission, reprinted.

Following the other thermodynamic paths indicated in Fig. 13 renders a distinct scenario. Figure 17 shows the film thickness y/a versus temperature T for two values of $\mathcal{C}_3 > \mathcal{C}_3^{tce}$ (green curve and violet curve) at $\Delta\mu_+/K = -1.07\times10^{-4}$. [As a reference, we plot also the results for $\mathcal{C}_3 = \mathcal{C}_3^{tce}$ (black curve).] The maximum of each of these two curves occurs at a temperature close to the corresponding bulk demixing

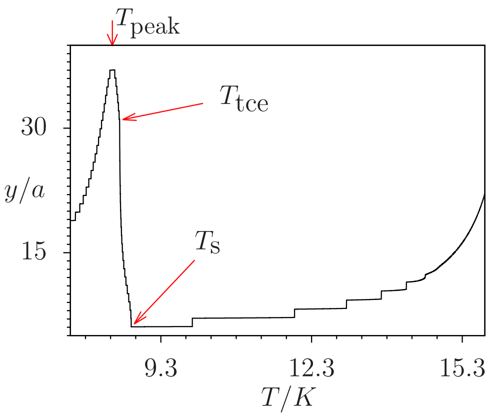

FIG. 15. Numerical results for the film thickness y/a corresponding to the thermodynamic path at fixed $\mathcal{C}_3 = \mathcal{C}_3^{\rm tce}$ and $\Delta\mu_+/K = -1.07\times10^{-4}$ (i.e., slightly shifted thermodynamic path shown by the vertical black dashed line in Fig. 13). The arrows indicate the tricritical end point $T_{\rm tce}$ and the onset temperature $T_{\rm s} \simeq T_{\rm s}(\mathcal{C}_3)$ for superfluidity at the surface transition. [The deviation of $T_{\rm s}$ from $T_{\rm s}(\mathcal{C}_3)$ (see Fig. 13) is due to the offset from liquid-vapor coexistence.] Below the tricritical temperature the thermodynamic path follows $T_{\rm d}^{\rm (s)}(\mathcal{C}_3)$ indicated in Fig. 13 (infinitesimally on the superfluid side). For further discussions see the main text. The bulk parameters of the system are those belonging to Figs. 4(c) and 13. $T_{\rm peak}/K = 8.3346$ is the position of the peak.

temperature denoted as $T_{\rm d}^{\rm (n)}(\mathcal{C}_3)$. [This slight deviation from $T_{\rm d}(\mathcal{C}_3)$ is due to the offset $\Delta\mu_+$ from the liquid-vapor coexistence surface.] The green curve corresponding to $\Delta\mathcal{C}_3 = \mathcal{C}_3 - \mathcal{C}_3^{\rm tce} = 0.0087$ joins the black one at $T/K \simeq T_{\rm d}^{\rm (n)}(\mathcal{C}_3)/K = 8.3925$; for lower temperatures both curves merge. Since for the green curve $T_{\rm d}^{\rm (n)}(\mathcal{C}_3) > T_{\rm peak} = 8.3346$, the maximum of this curve is the same as the maximum of the black curve. However, for $\Delta\mathcal{C}_3 = 0.0257$ the violet curve joins the black curve at the corresponding demixing temperature $T/K \simeq T_{\rm d}^{\rm (n)}(\mathcal{C}_3)/K = 8.2392$, which is below the temperature $T_{\rm peak}$ of the peak. Therefore, the maximum of the violet curve differs from the maximum of the black curve.

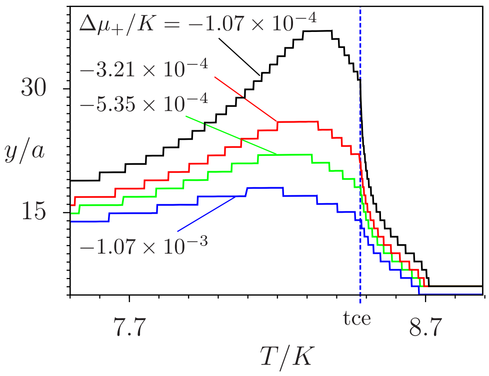

FIG. 16. Film thickness y/a versus temperature T at $\mathcal{C}_3 = \mathcal{C}_3^{\rm tce}$ for four values of $\Delta\mu_+/K$. By increasing the offset value $|\Delta\mu_+|$ the tricritical Casimir effect and complete wetting become less pronounced.

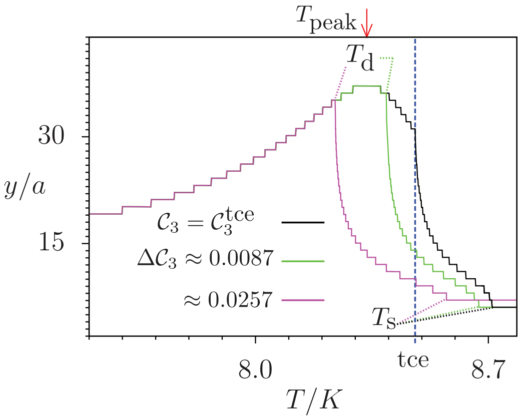

FIG. 17. Film thickness y/a as function of temperature T for three values of $\mathcal{C}_3 \geqslant \mathcal{C}_3^{\rm tce}$, i.e., $\Delta\mathcal{C}_3 = \mathcal{C}_3 - \mathcal{C}_3^{\rm tce} \geqslant 0$, and at $\Delta\mu_+/K = -1.07\times10^{-4}$. The sudden drop in the green and in the violet curve occurs at $T_{\rm d}$ close to the demixing temperature $T_{\rm d}^{\rm (n)}(\mathcal{C}_3)$ (see Fig. 13 with the same color code). Below $T_{\rm d}^{\rm (n)}(\mathcal{C}_3)$ the violet and the green curve merge with the black curve and follow the binodal denoted by $T_{\rm d}^{\rm (n)}(\mathcal{C}_3)$ in Fig. 13. The black curve is similar to the one in Fig. 15 except that below $T_{\rm tce}$ it follows the normal branch of the binodal [see Fig. 4(c)]. The jumps are due to first-order layering transitions. This figure corresponds to Fig. 14(a). Note that X and $X_{\rm t}$ in Fig. 14 here correspond to $\mathcal{C}_3$ and $\mathcal{C}_3^{\rm tce}$, respectively. Due to the offset from liquid-vapor coexistence the values of $T_{\rm d}$ and $T_{\rm s}$ differ slightly from $T_{\rm d}^{\rm (n)}(\mathcal{C}_3)$ and $T_{\rm s}(\mathcal{C}_3)$ as shown in Fig. 13. The bulk parameters of the system are the same as in Figs. 4(c) and 13. $T_{\rm peak}/K = 8.3346$ is the position of the peak.

Figure 17 corresponds to Fig. 14(a). Note that $X_{\rm t}$ in Fig. 14 corresponds to $\mathcal{C}_3^{\rm tce}$ in the present notation.

Figure 18 shows the film thickness as function of temperature for two values of $\mathcal{C}_3 < \mathcal{C}_3^{\rm tce}$ (red curve and blue curve; compare the inset in Fig. 13 with the same color code) and for $\mathcal{C}_3^{\rm tce}$ (black curve) at $\Delta\mu_+/K = -1.07\times10^{-4}$. The blue curve and the red curve merge with the black one at $T_{\rm d}$ close to the demixing temperature denoted as $T_{\rm d}^{\rm (s)}(\mathcal{C}_3)$ in Fig. 13 (there is a slight deviation due to the offset from the liquid-vapor coexistence). Whereas for $\mathcal{C}_3 \geqslant \mathcal{C}_3^{\rm tce}$ the sudden drop of the film thickness occurs near $T_{\rm d}^{\rm (n)}(\mathcal{C}_3)$ [note that for $T_{\rm d}^{\rm (s,n)}(\mathcal{C}_3^{\rm tce}) = T_{\rm tce}$], for $\mathcal{C}_3 < \mathcal{C}_3^{\rm tce}$ it takes place close to the bulk λ transition temperature $T_\lambda(\mathcal{C}_3) \geqslant T_{\rm tce}$. (Again, there is a slight deviation due to the offset from the liquid-vapor coexistence surface.) This sudden drop is associated with a break in slope in the curves $y(T)$ and leads to the formation of characteristic shoulders. This agrees with the experimental observations [see Fig. 14(b)]. Note that because $T_\lambda(\mathcal{C}_3)$ is a decreasing function of $\mathcal{C}_3$, for lower concentrations of ^{3}He, the break in slope occurs at higher temperatures. For the red curve in Fig. 18, this shoulder is due to the emerging of the CCFs close to the λ line. For even lower values of $\mathcal{C}_3$ the films encounter only the CCFs due to the λ transition, and the TCFs due to the tricritical point do not influence them (see the blue curve). In Fig. 18 all curves attain their lowest value at the surface transition temperature $T_{\rm s}(\mathcal{C}_3) > T_\lambda(\mathcal{C}_3)$.

For a vertical path at $\mathcal{C}_3 < \mathcal{C}_3^{\rm s*}$ (see Fig. 13), the film thickness does not exhibit an increase near the λ transition. In fact, for $\mathcal{C}_3 < \mathcal{C}_3^{\rm s*}$ the BCs for the superfluid OP at the interface of the

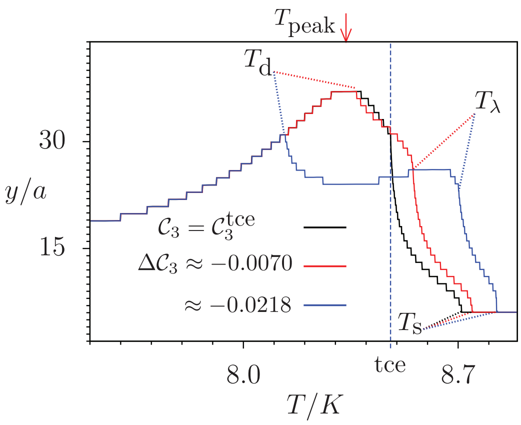

FIG. 18. Film thickness y/a as function of temperature T for three values of $\mathcal{C}_3 \leqslant \mathcal{C}_3^{\rm tce}$ with $\Delta\mathcal{C}_3 = \mathcal{C}_3 - \mathcal{C}_3^{\rm tce} \leqslant 0$ and at $\Delta\mu_+/K = -1.07\times10^{-4}$. The black curve is the same as the one in Fig. 15. The sudden drop in the blue and in the red curve occurs at T_λ close to the temperature of the λ transition $T_\lambda(\mathcal{C}_3)$ (see Fig. 13). The red and the blue curve merge with the black curve at $T_{\rm d}$ and follow the binodal denoted by $T_{\rm d}^{(s)}(\mathcal{C}_3)$ in Fig. 13. This figure corresponds to panel (b) in Fig. 14. Note that X and $X_{\rm t}$ in Fig. 14 here correspond to $\mathcal{C}_3$ and $\mathcal{C}_3^{\rm tce}$, respectively. Due to the offset from liquid-vapor coexistence the value of $T_{\rm d}$, $T_{\rm s}$, and T_λ differ slightly from $T_{\rm d}^{(s)}(\mathcal{C}_3)$, $T_{\rm s}(\mathcal{C}_3)$, and $T_\lambda(\mathcal{C}_3)$ as introduced in Fig. 13. The bulk parameters of the system are the same as in Figs. 4(c) and 13. $T_{\rm peak}/K = 8.3346$ is the position of the peak.

wetting film are the symmetric (O,O) BCs (i.e., $M = 0$ at the wall and at the emerging liquid-vapor interface). Therefore, in this regime one expects the occurrence of an *attractive* CCF; however, above the bulk critical point this cannot be captured within the present mean field approximation because for Dirichlet-Dirichlet BCs the resulting CCF is solely due to fluctuations beyond mean field theory [15,16]. Although both black curves in Figs. 17 and 18 correspond to $\mathcal{C}_3 = \mathcal{C}_3^{\rm tce}$, they differ slightly due to the infinitesimal difference of the thermodynamic paths for $T < T_{\rm tce}$. In Fig. 17, for $T < T_{\rm tce}$ the thermodynamic paths follow the demixing line $T_{\rm d}^{(n)}(\mathcal{C}_3)$ infinitesimally on the normal fluid side, whereas in Fig. 18 for $T < T_{\rm tce}$ the thermodynamic paths run along the superfluid binodal $T_{\rm d}^{(s)}(\mathcal{C}_3)$.

C. Tricritical Casimir forces

A fluid film exerts an effective force on its confining walls. For two parallel, planar walls a distance L apart this fluid mediated force f_s is given by [40]

$$f_s = -\left(\frac{\partial \mathcal{F}^{\rm ex}}{\partial L}\right)_{T,\mu} = -\left[\frac{\partial(\mathcal{F} - V f_{\rm b})}{\partial L}\right]_{T,\mu}, \qquad (20)$$

where $\mathcal{F}^{\rm ex}$ is the excess free energy, $f_{\rm b}$ is the grand canonical bulk free energy density of a one-component fluid at temperature T and chemical potential μ. $\mathcal{F}$ is the free energy of the film of volume $V = \mathcal{A}L$ where $\mathcal{A}$ is the macroscopically large surface area of one wall. Since $\mathcal{F} - V f_b$ is proportional to $\mathcal{A}$, $f_s/\mathcal{A}$ is the pressure in excess over its bulk value. Upon approaching the bulk critical point of the confined fluid, f_s acquires a *universal* long-ranged contribution f_C, known as the critical Casimir force [18,41,42].

Extending this concept to binary liquid mixtures, here we focus on that contribution to $f_{\rm s}$ which arises near a tricritical point of ^{3}He-^{4}He mixtures. We call this contribution tricritical Casimir force $F_{\rm TCF}$ (TCF) and express it in units of $k_{\rm B}T_{\rm tc}$, where $T_{\rm tc}$ is the temperature of a tricritical point on the line TC in Fig. 1.

As discussed in the Introduction, concerning wetting by a critical fluid, the critical fluctuations of the OP are confined by the solid substrate surface on one side and by the emerging liquid-vapor interface on the other side. Accordingly, the TCF is the derivative of the corresponding excess free energy with respect to the film thickness y at constant temperature and chemical potentials. In contrast to the slab geometry with two fixed walls as discussed above [see Eq. (20)], varying the equilibrium wetting film thickness requires to change the thermodynamic state of the fluid. Moreover, in the present microscopic approach the film thickness is not an input parameter of a model; hence, the excess free energy is not an explicit function of y. [Note that y is uniquely defined in terms of the equilibrium density profile $D_l(T,\mu_+,\mu_-)$ via Eq. (18).] In order to calculate the TCF, we consider a system at fixed T,μ_+, and μ_-, for which the film thickness is fixed to a specific value ℓ by an externally imposed constraint. For the total free energy $F_{\rm cstr}$ of such a constraint system, one has for large L [1,16,43]

$$\begin{aligned} &F_{\rm cstr}(T,\mu_+,\mu_-,\ell)/A \\ &\quad = f_{\rm m}\ell + f_{\rm b}(L-\ell) + \sigma_{\rm w,l} + \sigma_{\rm l,v} + f_{\rm ex}(\ell), \end{aligned} \qquad (21)$$

where $\sigma_{\rm w,l}$ and $\sigma_{\rm l,v}$ are the wall-liquid and vapor-liquid surface tensions, respectively, $f_{\rm m}$ is the free energy density of the metastable liquid, and $A := \mathcal{N}a^2$ is the cross section area of a layer. Since at liquid-vapor coexistence $f_{\rm b} = f_{\rm vapor} = f_{\rm liquid} < f_{\rm m}$ one has $(f_{\rm m} - f_{\rm b})\ell > 0$. The ℓ-dependent excess free energy $f_{\rm ex}(\ell)$ is the sum of two contributions: the free energy density (per area A) $f_0(\ell)$ due to the effective interaction of the emerging liquid-vapor interface with the substrate wall and the singular contribution $f_{\rm sing}(\ell)$ due to the critical finite-size effects within the wetting film of thickness ℓ. For short-ranged surface fields, the effective potential between the wall and the emerging liquid-vapor interface is an exponentially decaying function of the film thickness ℓ. To leading order one has [44]

$$f_0(\ell) \approx \alpha\frac{T - T_w}{T_w}\exp(-p\ell), \qquad (22)$$

where T_w is the wetting transition temperature and $\alpha > 0$ is an amplitude such that in accordance with complete wetting (i.e., for $T > T_w$) $f_0(\ell) > 0$. The decay length $1/p$ is the bulk correlation length of the liquid at T_w and at liquid-vapor coexistence. With the knowledge of $f_{\rm ex}(\ell)$ and $f_0(\ell)$ one can determine the TCF as the negative derivative of $f_{\rm ex}(\ell) - f_0(\ell)$ with respect to ℓ. Since $y(T,\mu_+,\mu_-)$ is the equilibrium film thickness, the total free energy $F_{\rm cstr}$ has a global minimum at y, so that $\frac{\partial F_{\rm cstr}}{\partial \ell}|_{\ell=y} = 0$. Thus taking the derivative of both sides of Eq. (21) with respect to ℓ at $\ell = y$ yields

$$0 = f_{\rm m} - f_{\rm b} + \left.\frac{\partial f_0}{\partial \ell}\right|_{\ell=y} + \left.\frac{\partial f_{\rm sing}}{\partial \ell}\right|_{\ell=y}. \qquad (23)$$

With Eq. (22) this implies for the TCF per area f_{TCF}

$$f_{\mathrm{TCF}}(y) = -\left.\frac{\partial f_{\mathrm{sing}}}{\partial \ell}\right|_{\ell=y} \approx f_{\mathrm{m}} - f_{\mathrm{b}} - \alpha p \frac{T - T_w}{T_w} e^{-py}. \qquad (24)$$

The parameters α, T_w, and p can be determined by studying the growth of the equilibrium film thickness as a function of the chemical potential sufficiently far above the critical demixing region, where $f_{\mathrm{TCF}}(y)$ is negligible. Using Eq. (24) and calculating f_{m} and f_{b} within the present model, we have found that for the surface fields $(\tilde{f}_+, \tilde{f}_-)/K = (10.714, 16.071)$ and the coupling constants $(C/K, J/K, J_s/K) = (1, 9.107, 3.701)$, one has $T_w/K \simeq 3.704$, whereas $\alpha \simeq 1.146$, and $p \simeq 1.997$. We have checked that the value of the bulk correlation length $1/p$ agrees with the one following from the decay of the OP profiles.

In the slab geometry considered in Refs. [20,21], the total number density of the ^{3}He-^{4}He mixtures is fixed and the properties of the system near the bulk tricritical point can be expressed in terms of the experimentally accessible thermodynamic fields $T - T_{\mathrm{tc}}$ and $\mu_- - \mu_-^{\mathrm{tc}}$, where μ_-^{tc} is the value of μ_- at the tricritical point. (The thermodynamic field conjugate to the superfluid OP is experimentally not accessible and is omitted here.) As discussed in detail in Refs. [20,21,45], the proper dimensionless scaling fields are $t \equiv (T - T_{\mathrm{tc}})/T_{\mathrm{tc}}$ and $g \equiv (\mu_- - \mu_-^{\mathrm{tc}})/(k_B T_{\mathrm{tc}}) + a't$, where a' is the slope of the line tangential to the phase boundary curve at T_{tc} within the blue surface in Fig. 1 (i.e., parallel to the intersection of the blue surface and A$_4$ at tc which is the full blue horizontal line through tc). For such a choice of the scaling fields, for $t \to 0$ with $g = 0$ the tricritical point is approached tangentially to the phase boundary. According to finite-size scaling [11] the CCF for the slab of width L is governed by a universal scaling function defined as $\tilde{\vartheta}_{+,O} \simeq L^3 f_{\mathrm{TCF}}/(k_B T_{\mathrm{tc}})$, where the subscript $\{+, O\}$ denotes the surface universality classes of the confining surfaces (the symbol "$\simeq$" indicates asymptotic equality). The scaling function $\tilde{\vartheta}_{+,O}$ depends on the two scaling fields $c_1 t L^{1/\nu}$ and $c_2 g L^{\Delta/\nu}$, where c_1 and c_2 are nonuniversal metric factors and $\nu = 1$ and $\Delta = 2$ are tricritical exponents for the XY model in $d = 3$ [46]. In order to facilitate a comparison with experimental data, the results for the TCF obtained in Refs. [20,21] have been presented in terms of $\tilde{\vartheta}_{+,O}$ as a function of only the single scaling variable $c_1 t L^{1/\nu}$, with $c_1 = \xi_0^+/a$; ξ_0^+ (in units of a) is the amplitude of the superfluid OP correlation length $\xi = \xi_0^+ t^{-\nu}$ above T_{tc}. In Refs. [20,21], for thermodynamic paths of constant concentration, the influence of the variation of the second scaling variable g upon changing temperature has been neglected.

In the present case of TCF emerging in wetting films of thickness y, the TCF per area is given by the universal scaling function $\vartheta_{+,O}$ as

$$f_{\mathrm{TCF}}/(k_{\mathrm{B}} T_{\mathrm{tce}}) \simeq y^{-d} \vartheta_{+,O}(c_1 y t^{\nu}), \qquad (25)$$

with $t = (T - T_{\mathrm{tce}})/T_{\mathrm{tce}}$, where we have again neglected the dependence of $\vartheta_{+,O}$ on the scaling variable $c_2 g y^{\Delta/\nu}$ as well as on the third scaling variable associated with $\mu_+ - \mu_+^{\mathrm{tce}}$ which is conjugate to the total number density of the ^{3}He-^{4}He mixture. In order to retrieve, however, the full information stored in the scaling function, in principle one has to plot the scaling function as a function of a single scaling variable, while keeping all the other scaling variables fixed. In practice this is difficult to realize. Along the thermodynamic paths taken experimentally in Ref. [3], none of the scaling variables were fixed. Instead the scaling functions have been plotted versus the single scaling variable td, where in Ref. [3] d denotes the film thickness. We follow this experimentally inspired approach and plot $y^3 f_{\mathrm{TCF}}/(k_{\mathrm{B}} T_{\mathrm{tce}})$ as a function of yt, ignoring the nonuniversal metric factor c_1. Since the surfaces fields we have chosen for our calculation of the TCF are strong, we neglect the dependence of the scaling function on the corresponding scaling variables, assuming that for $(\tilde{f}_+, \tilde{f}_-)/K = (10.714, 16.071)$ the system is close to the fixed point (+) BC.

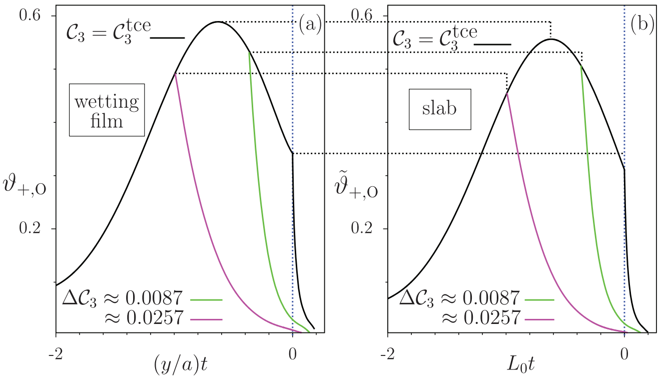

FIG. 19. Scaling functions of the TCF calculated from the data in Fig. 17 within (a) the wetting film geometry and (b) the slab approximation. Concerning the definition of the slab thickness L_0 see the main text. The violet curve and the green curve merge with the black curve at their corresponding demixing point indicated by T_{d} in Fig. 17, using the same color code. The corresponding curves in the two panels agree qualitatively but differ in detail, e.g., in height (see the horizontal lines). In panel (a) the thermodynamic states are off the liquid-vapor coexistence surface, whereas in panel (b) the thermodynamic states lie on the liquid-vapor coexistence surface. The reduced temperature is $t = (T - T_{\mathrm{tce}})/T_{\mathrm{tce}}$, where T_{tce} is the temperature of the tricritical end point. Due to the smoothing procedure and within the presently available numerical accuracy, the small difference between the positions of the maxima in (a) and (b) cannot be resolved reliably.

Figures 19(a) and 20(a) show the scaling functions calculated from the data in Figs. 17 and 18, respectively. In order to eliminate the nonuniversal features arising from the jumps in the wetting films due to the layering transitions, these curves have been smoothed. Figure 21(a) shows the scaling functions for various values of $\Delta\mu_+$ corresponding to the various curves in Fig. 16. The vertical blue dotted line in Figs. 19–21 represents the tricritical end point ($t = 0$). Away from the tricritical temperature the scaling functions decay to zero. This decay is faster for temperatures higher than the tricritical temperature, i.e., for $t > 0$. For $t > 0$ the dashed section of the blue curve in Fig. 20 shows that part, which is multivalued. This indicates that in this range of the scaling variable the scaling hypothesis is not applicable. The same holds also for the red curve in this figure, where the sudden drop exhibits a slightly positive slope.

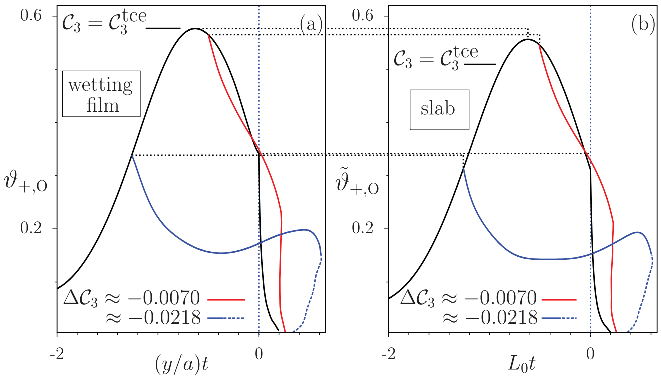

FIG. 20. Scaling functions of the TCF calculated from the data in Fig. 18 within (a) the wetting film geometry and (b) the slab approximation. Concerning the definition of the slab thickness L_0 see the main text. The blue curve and the red curve merge with the black curve at their corresponding demixing point, indicated by T_d in Fig. 18. The corresponding curves in the two panels agree qualitatively but differ in detail, e.g., in height (see the horizontal lines). The dashed blue curve shows the region, where the blue curve is multivalued and scaling does not hold anymore. The same holds also for the right parts of the red curves, because the drops of the curves exhibit a slightly positive slope. In panel (a) the thermodynamic states are off the liquid-vapor coexistence surface, whereas in panel (b) the thermodynamic states lie on the liquid-vapor coexistence surface. The reduced temperature is $t = (T - T_{\rm tce})/T_{\rm tce}$, where $T_{\rm tce}$ is the temperature of the tricritical end point. Due to the smoothing procedure and within the presently available numerical accuracy, the small difference between the positions of the maxima in (a) and (b) cannot be resolved reliably.

In order to compare our wetting results for the TCF with those obtained in the slab geometry as studied in Refs. [20,21], we employ a suitable slab approximation for our wetting data. To this end we consider a slab of width L_0 equal to the equilibrium position of the emerging liquid-vapor interface of the wetting film $L_0(T,\mu_+,\mu_-) = \lfloor y(T,\mu_+,\mu_-)\rfloor$, at a certain value of the offset $\Delta\mu_+$. Since within the present lattice model the system size L_0 must be an integer, the above assignment for L_0 involves the floor function $\lfloor\quad\rfloor$. ($\lfloor x\rfloor$ gives the largest integer number smaller than x.)

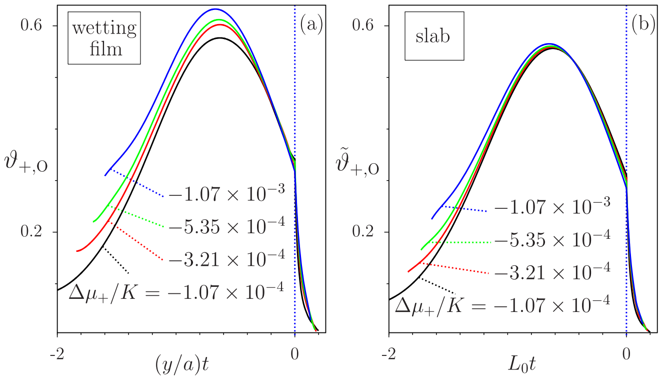

FIG. 21. Scaling functions of the TCF calculated from the data in Fig. 16 within (a) the wetting film geometry and (b) the slab approximation. Concerning the definition of the slab thickness L_0 see the main text. The maxima of the scaling functions in panel (a) differ from each other, whereas the ones in panel (b) are almost equal. The reduced temperature is $t = (T - T_{\rm tce})/T_{\rm tce}$, where $T_{\rm tce}$ is the temperature of the tricritical end point.

Within the slab approximation, the emerging liquid-vapor interface is replaced by a wall (denoted by "2") with the short-ranged surface fields $\tilde{f}_{+,2}$ and $\tilde{f}_{-,2}$. These surface fields are chosen such that the OP profiles calculated for the slab *at* liquid-vapor coexistence (i.e., $\Delta\mu_+ = 0$) resembles the ones within the wetting film geometry calculated for the semi-infinite system with an offset $\Delta\mu_+ < 0$. In order to obtain a perfect match, one would have to allow these surface fields to vary along the thermodynamic paths taken. Insisting, however, on fixed values of $(\tilde{f}_{+,2},\tilde{f}_{-,2})$, we have found that for $(\tilde{f}_{+,2},\tilde{f}_{-,2})/K = (1.607,0.214)$ the profiles in the slab geometry agree rather well with their counterparts in the wetting film geometry. For $(\tilde{f}_{+,2},\tilde{f}_{-,2})/K = (1.607,0.214)$ the number density $X_{4,l}$ of ^{4}He at the right boundary is not high enough for the spontaneous symmetry breaking of the superfluid OP to occur there. On the contrary, for $(\tilde{f}_{+},\tilde{f}_{-})/K = (10.714,16.071)$ at the left boundary M_l is nonzero. Accordingly, the two sets of surface fields induce $(+,O)$ and thus nonsymmetric BCs on the superfluid OP within the slab, giving rise to repulsive TCFs. For such a slab, by using Eq. (20) we calculate the TCF for that bulk thermodynamic state which is associated with the wetting film, but taken *at* bulk liquid-vapor coexistence (i.e., $\Delta\mu_+ = 0$). In this way we can mimic the actual experimental wetting situation and stay consistent with the calculations for the slab geometry as carried out in Refs. [20,21]. Within lattice models, the smallest change in the system size amounts to one layer $[\min(\Delta L_0) = 1]$. Therefore, on the lattice the derivative in Eq. (20) has to be approximated by the finite difference

$$f_{\rm TCF} = -\frac{\Delta f^{\rm ex}(L_0)}{\Delta L_0} = -[f^{\rm ex}(L_0+1) - f^{\rm ex}(L_0)], \qquad (26)$$

where $f^{\rm ex} = \mathcal{F}^{ex}/A$. In order to determine $f^{\rm ex}(L_0)$, we write the total free energy ϕ of the slab within thickness L_0 as

$$\phi(L_0,T,\mu_+,\mu_-)/A = f_{\rm b}L_0 + \sigma_{\rm s,l}^{(1)} + \sigma_{\rm s,l}^{(2)} + f^{\rm ex}(L_0), \qquad (27)$$

where $\sigma_{\rm s,l}^{(1)}$ and $\sigma_{\rm s,l}^{(2)}$ are the surface tensions between the liquid and surface (1) and surface (2), respectively. The surface tensions are functions of T,μ_+, and μ_- only and do not depend on the system size L_0. Using Eq. (27), Eq. (26) can be expressed as

$$f_{\rm TCF} = [\phi(L_0) - \phi(L_0+1)]/A + f_{\rm b}. \qquad (28)$$

Figures 19(b), 20(b), and 21(b) show the scaling functions $\tilde{\vartheta}_{+,O}$ within the slab approximation, corresponding to the cases in panel (a) of each figure. Also here curves have been smoothed out in order to eliminate the discontinuities due to the layering transitions. The approximation of the derivative in Eq. (26) by a finite difference and a slight mismatch between the OP profiles in the slab and in the wetting film produce deviations in amplitude of the scaling functions comparable to the ones in panel (a) of each figure. In addition, these deviations might be caused by the difference between the thermodynamic paths taken in the two panels. In Fig. 20(b) the dashed section of the blue curve (with $t > 0$) shows that part, for which the scaling hypothesis breaks down. This occurs for very small values of L_0, in particular above the tricritical end point, where the wetting film thickness is small,. This is in line with the general rule that universal scaling functions only hold in the scaling limit $L_0 \gg a$.

IV. SUMMARY AND CONCLUSIONS

By using mean field theory, layering transitions, wetting films, and tricritical Casimir forces (TCFs) in ^{3}He-^{4}He mixtures have been studied within the vectorized Blume-Emery-Griffiths model on a semi-infinite, simple cubic lattice. In the bulk, the model reduces to the one studied in Ref. [33]. For vanishing coupling constant J_s, which facilitates superfluid transitions, the bulk phase diagram corresponds to that of classical binary liquid mixtures [Figs. 4(a) and 5]. We have identified those values of J_s (see Fig. 23), for which the bulk phase diagram resembles that of actual ^{3}He-^{4}He mixtures [Figs. 4(b) and 4(c) and Fig. 1].

The present model includes short-ranged surface fields f_+ and f_- coupled to the sum and to the difference of the number densities of ^{3}He and ^{4}He atoms, respectively, which allows for the occurrence of wetting phenomena and can control the preference of the surfaces for the species. The effect of the surface fields on wetting films has been studied for $J_s = 0$. Depending on the values of f_+ and f_-, in the vapor phase very close to liquid-vapor coexistence, the model exhibits incomplete or complete wetting (Figs. 6–8). Due to the lattice character of the present model, we observe also first-order layering transitions (Figs. 9 and 10).

For suitable values of the surface fields and for the coupling constants, which determine the bulk phase diagram of the ^{3}He-^{4}He mixtures, we have been able to reproduce qualitatively the experimental results (see Fig. 14) for the thickness of ^{3}He-^{4}He wetting films near the tricritical end point [3]. Although the measurements in Refs. [3] have been performed in the regime of complete wetting, due to gravity the thickness of the wetting films remained finite. In the present study this is achieved by applying an offset to the experimental thermodynamic paths (Fig. 2) and shifting them into the vapor phase so that the resulting wetting films remain finite (Figs. 1 and 3). Within the present mean field approach the order parameter profiles at a given thermodynamic state provide all equilibrium properties of the wetting films (Fig. 12). The closer the system to liquid-vapor coexistence is, the thicker the wetting films are (Fig. 11). Depending on the thermodynamic state, the wetting films can be superfluid. For the bulk phase corresponding to the normal fluid, the onset of superfluidity occurs by crossing a line of continuous surface transitions (Fig. 13).

Taking thermodynamic paths (Fig. 13) equivalent to the experimental ones taken in Ref. [3], we have been able to reproduce qualitatively the experimental results for the variation of the film thickness upon approaching the tricritical end point. Since the tricritical end point lies between the wetting temperature and the critical point of the liquid-vapor phase transitions, there is a pronounced change in the thickness of the wetting film due to repulsive TCFs (Figs. 15–18). The repulsive nature of the TCF is due to the effectively nonsymmetric boundary conditions for the superfluid OP. The nonsymmetric boundary conditions arise due to the formation of a ^{4}He-rich layer near the solid-liquid interface, which can become superfluid even at temperatures above the λ transition; at the liquid-vapor interface such a superfluid layer does not form because the ^{4}He concentration is too low there. This leads to $(+,O)$ boundary conditions. Such boundary conditions hold below the line $T_s(\mathcal{C}_3)$ of surface transitions (blue curve in Fig. 13) up to the special point s^* (i.e., for $\mathcal{C}_3 > \mathcal{C}_3^{s^*}$). Like the experiment data, upon decreasing the temperature along the thermodynamic paths at fixed $\mathcal{C}_3$ in the region $\mathcal{C}_3^{s^*} < \mathcal{C}_3 < \mathcal{C}_3^{\mathrm{tce}}$, in addition to the repulsive TCFs close to tce the wetting films, are also influenced by the repulsive critical Casimir forces (CCFs) close to the λ line $T_\lambda(\mathcal{C}_3)$ (red line in Fig. 13). This gives rise to the formation of a shoulderlike curve in Figs. 18 and 14(b) between the tricritical end point and the λ transition temperature. For $\mathcal{C}_3 < \mathcal{C}_3^{s^*}$ the wetting film resembles that of pure ^{4}He, for which the superfluid order parameter vanishes both at the solid substrate and at the liquid-vapor interface. Such symmetric (O,O) boundary conditions lead to an attractive CCF, which results in the decrease of the wetting film thickness close to the λ transition temperature $T_\lambda(\mathcal{C}_3)$ [see the dip in Fig. 14(c)]. However, because the attractive CCF due to (O,O) boundary conditions is generated by fluctuations only [16] above the bulk critical point it cannot be captured within the present mean field approach.

Using the various contributions to the total free energy, one can calculate the TCFs and their scaling function by extracting the excess free energy from the total free energy [Figs. 19(a), 20(a), and 21(a)]. We have adapted the slab approximation for the wetting films to the present system and have calculated the corresponding slab scaling function of the TCF [Figs. 19(b), 20(b), and 21(b)]. We have found that the slab approximation, with fixed surface fields at the second wall mimicking the emerging liquid-vapor interface, captures rather well the qualitative behavior of the scaling functions inferred from the wetting film thickness [see the comparison between the panels (a) and (b) in Figs. 19–21].

We conclude by comparing the scaling function inferred from the wetting film thickness and the one calculated within the slab geometry as in Refs. [20,21] with the experimental data [3], specifically at the tricritical concentrations $\mathcal{C}_3^{\mathrm{tce}}$ of ^{3}He. Figure 22 illustrates this comparison. $\overline{L}$ refers to the wetting film thickness measured in the experimental data or calculated within the present model. In Refs. [20,21] $\overline{L}$ refers to the slab width. In the reduced temperature $t = (T - T_{\mathrm{tc}})/T_{\mathrm{tc}}$, T_{tc} refers to the temperature of the tricritical end point both in the present calculation and in the experimental studies, whereas it denotes the tricritical temperature in Refs. [20,21]. The theoretical scaling functions are rescaled such that their values at $t = 0$ match the experimental one. Moreover, the scaling variable $x = t\overline{L}$ for the theoretical results is multiplied by a suitable factor such that the positions of the maxima of the theoretical curves match the experimental one. This factor is $b_{\mathrm{th}} \simeq 23.1$ for the wetting film, whereas for the slab geometry it is $b_{\mathrm{th}}^{\mathrm{VBEG}} \simeq 15.38$. The resulting adjusted scaling functions $\overline{\vartheta}_{+,O}(x)$ agree with each other and reproduce rather well the experimental data, especially near the maximum. In contrast, if these two adjustments of the scaling function is enforced for

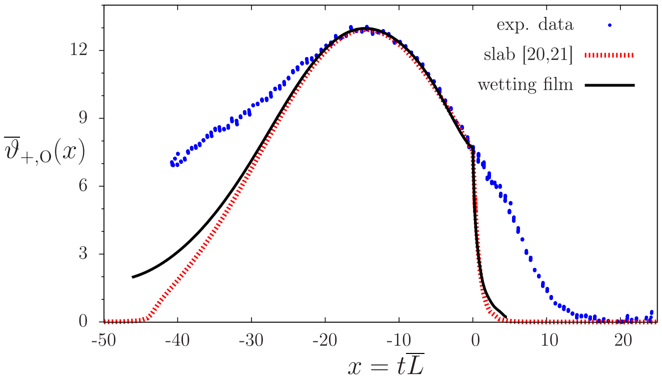

FIG. 22. Adjusted scaling functions (see the main text) obtained for the slab geometry as in Refs. [20,21] and inferred from the wetting films compared with the corresponding experimental curve [3]. All data correspond to the tricritical concentration of ^{3}He. $\overline{L}$ is the film thickness of the wetting films, whereas in Refs. [20,21] it denotes the width of the slab. The reduced temperature $t = (T - T_{\mathrm{tc}})/T_{\mathrm{tc}}$ is relative to tricritical point in Refs. [20,21] and relative to the tricritical end point for the wetting film. The experimental data has been obtained via private communication with the corresponding authors.

the one obtained within the slab approximation inferred from the wetting films [i.e., the black curve in Fig. 20(b)], there is no satisfactory agreement with the experimental data as a whole (this adjusted scaling function is not shown in Fig. 22).

The present model lends itself to further investigations based on Monte Carlo simulations. They would capture the effects of fluctuations beyond the present mean field theory. Since the upper critical dimension for tricritical phenomena is $d^* = 3$, this would shed additional light on the reliability of the present mean field analysis. Moreover, in view of the ubiquity of van der Waals interactions it will be rewarding to extend the present model by incorporating long-ranged surface fields.

ACKNOWLEDGMENTS

N.F.B. would like to thank Dr. Markus Bier and Dr. Piotr Nowakowski for fruitful discussions.

APPENDIX A: MEAN FIELD APPROXIMATION FOR THE LATTICE MODEL

In this Appendix we present the details of the calculations outlined in Sec. II A. The starting point is the Hamiltonian in Eq. (3). According to the variation principle, the equilibrium free energy F obeys the inequality [47]

$$F \leqslant \phi = \hat{\mathrm{Tr}}(\rho \mathcal{H}) + (1/\beta)\hat{\mathrm{Tr}}(\rho \ln \rho), \tag{A1}$$

where ρ is any trial density matrix fulfilling $\hat{\mathrm{Tr}}(\rho) = 1$, with respect to which ϕ on the right-hand-side of Eq. (A1) has to be minimized in order to obtain the best approximation for F:

$$\hat{\mathrm{Tr}} = \sum_{s_1=\pm1,0} \int_0^{2\pi} d\Theta_1 \cdot \cdots \cdot \sum_{s_{L\mathcal{N}}=\pm1,0} \int_0^{2\pi} d\Theta_{L\mathcal{N}} \tag{A2}$$

denotes the trace and $\beta = 1/T$ where T is the temperature times k_{B}. Within mean field theory, the total density matrix of the system factorizes as

$$\rho = \prod_{i=1}^{L\mathcal{N}} \rho_i = \prod_{l=0}^{L-1} \prod_{\nu_l=1}^{\mathcal{N}} \rho_{(l,\nu_l)} \tag{A3}$$

with

$$\mathrm{Tr}\rho_{(l,\nu_l)} = \sum_{s_{(l,\nu_l)}=\pm1,0} \int_0^{2\pi} d\Theta_{(l,\nu_l)} \rho_{(l,\nu_l)}(s_{(l,\nu_l)}, \Theta_{(l,\nu_l)}) = 1, \tag{A4}$$

where l labels the L layers, ν_l denotes the lattice sites within the lth layer, and $\rho_{(l,\nu_l)}$ denotes the density matrix of lattice site ν_l within the layer l. (Note that $\hat{\mathrm{Tr}}$ denotes the trace over all degrees of freedom, whereas Tr refers to the trace over the degrees of freedom at a single lattice site.)

By applying mean field approximation to the sites within each layer, $\rho_{(l,\nu_l)}$ is taken to be independent of ν_l. Accordingly, Eq. (A3) renders

$$\rho = \prod_{l=0}^{L-1} \rho_l^{\mathcal{N}} \tag{A5}$$

with

$$\mathrm{Tr}\rho_l = \sum_{s_l=\pm1,0} \int_0^{2\pi} d\Theta_l \rho_l(s_l, \Theta_l) = 1, \tag{A6}$$

where $\rho_l \equiv \rho_{(l,\nu_l)}$ indicates the density matrix for a single site in the lth layer; $s_l \equiv s_{(l,\nu_l)}$ and $\Theta_l \equiv \Theta_{(l,\nu_l)}$ denote the occupation variable and the angle for a single site within this layer, respectively, independent of ν_l. [Note that due to the definitions in Eq. (5), one has $q_l \equiv q_{(l,\nu_l)}$ and $p_l \equiv p_{(l,\nu_l)}$.] The summations in Eq. (3) can be written as

$$\sum_{i=1}^{L\mathcal{N}} = \sum_{l=0}^{L-1} \sum_{\nu_l=1}^{\mathcal{N}} = \mathcal{N} \sum_{l=0}^{L-1} \tag{A7}$$

and

$$\begin{aligned} \sum_{\langle i,j \rangle} &= \frac{1}{2} \sum_{i=1} \left\{ \sum_{j \in \mathrm{n.n.}(l)} + \sum_{j \in \mathrm{n.n.}(l+1)} + \sum_{j \in \mathrm{n.n.}(l-1)} (1 - \delta_{l,0}) \right\} \\ &= \frac{\mathcal{N}}{2} \sum_{l=0}^{L-1} \left\{ 4 + \sum_{j \in \mathrm{n.n.}(l+1)} + \sum_{j \in \mathrm{n.n.}(l-1)} (1 - \delta_{l,0}) \right\}, \end{aligned} \tag{A8}$$

where n.n.(l), n.n.$(l+1)$, and n.n.$(l-1)$ denote the nearest neighbors in the layers l, $l+1$, and $l-1$, respectively. The factor $1/2$ prevents double counting and the factor $(1 - \delta_{l,0})$ appears due to the fact that layer $l = 0$ next to the surface does not have a neighboring layer at $l = -1$. Since the lattice sites within each layer are equivalent one has $\sum_{j \in \mathrm{n.n.}(l)} = 4$.

By using Eq. (3) together with the above considerations, Eq. (A1) renders

$$\begin{aligned} \phi = &- \frac{K\mathcal{N}}{2} \sum_{l=0}^{L-1} \langle s_l \rangle [4\langle s_l \rangle + \langle s_{l+1} \rangle + \langle s_{l-1} \rangle (1 - \delta_{l,0})] \\ &- \frac{J\mathcal{N}}{2} \sum_{l=0}^{L-1} \langle q_l \rangle [4\langle q_l \rangle + \langle q_{l+1} \rangle + \langle q_{l-1} \rangle (1 - \delta_{l,0})] \end{aligned}$$

$$
\begin{aligned}
&-\frac{C\mathcal{N}}{2}\sum_{l=0}^{L-1}\langle s_l\rangle[4\langle q_l\rangle+\langle q_{l+1}\rangle+\langle q_{l-1}\rangle(1-\delta_{l,0})]\\
&-\frac{C\mathcal{N}}{2}\sum_{l=0}^{L-1}\langle q_l\rangle[4\langle s_l\rangle+\langle s_{l+1}\rangle+\langle s_{l-1}\rangle(1-\delta_{l,0})]\\
&-\frac{J_s\mathcal{N}}{2}\sum_{l=0}^{L-1}\langle p_l\cos\Theta_l\rangle[4\langle p_l\cos\Theta_l\rangle\\
&+\langle p_{l+1}\cos\Theta_{l+1}\rangle+\langle p_{l-1}\cos\Theta_{l-1}\rangle(1-\delta_{l,0})]\\
&-\frac{J_s\mathcal{N}}{2}\sum_{l=0}^{L-1}\langle p_l\sin\Theta_l\rangle[4\langle p_l\sin\Theta_l\rangle+\langle p_{l+1}\sin\Theta_{l+1}\rangle\\
&+\langle p_{l-1}\sin\Theta_{l-1}\rangle(1-\delta_{l,0})]\\
&-\mathcal{N}\mu_-\sum_{l=0}^{L-1}\langle s_l\rangle-\mathcal{N}\mu_+\sum_{l=0}^{L-1}\langle q_l\rangle-\mathcal{N}\sum_{l=0}^{L-1}\langle f_-(l)s_l\rangle\\
&-\mathcal{N}\sum_{l=0}^{L-1}\langle f_+(l)q_l\rangle+(1/\beta)\left\langle\ln\prod_{l=0}^{L-1}\rho_l^{\mathcal{N}}\right\rangle, \qquad \text{(A9)}
\end{aligned}
$$

where $\langle\ldots\rangle=\mathrm{Tr}(\rho_l\ldots)$ denotes the thermal average taken with the trial density matrix ρ_l associated with a single lattice site in layer l.

The last term in Eq. (A9) can be written as

$$
(1/\beta)\left\langle\ln\prod_{l=0}^{L-1}\rho_l^{\mathcal{N}}\right\rangle=(\mathcal{N}/\beta)\left\langle\sum_{l=0}^{L-1}\ln\rho_l\right\rangle. \qquad \text{(A10)}
$$

Minimizing the variational function $\phi/\mathcal{N}$ with respect to ρ_l renders the best normalized functional form of ρ_l among the single-site, factorized density matrices. Thus we determine the functional derivative of $\phi/\mathcal{N}$ in Eq. (A9) with respect to $\rho_l(s_l,\Theta_l)$ using $\frac{\delta\rho_l(s_l,\Theta_l)}{\delta\rho_{l'}(s'_{l'},\Theta'_{l'})}=\delta_{l,l'}\delta(\Theta_l-\Theta'_{l'})\delta_{s_l,s'_{l'}}$, and equate it to the Lagrange multiplier η corresponding to the constraint $\mathrm{Tr}(\rho_l)=1$:

$$
\begin{aligned}
\eta&=\frac{\delta(\phi/\mathcal{N})}{\delta\rho_l(s_l,\Theta_l)}\\
&=-K\{s_l[4X_l+X_{l+1}+X_{l-1}(1-\delta_{l,0})]\}\\
&\quad-J\{q_l[4D_l+D_{l+1}+D_{l-1}(1-\delta_{l,0})]\}\\
&\quad-C\{s_l[4D_l+D_{l+1}+D_{l-1}(1-\delta_{l,0})]\}\\
&\quad-C\{q_l[4X_l+X_{l+1}+X_{l-1}(1-\delta_{l,0})]\}\\
&\quad-[\mu_-+f_-(l)]s_l-[\mu_++f_+(l)]q_l\\
&\quad-J_s\big\{p_l\cos\Theta_l\big[4M_l^x+M_{l+1}^x+M_{l-1}^x(1-\delta_{l,0})\big]\big\}\\
&\quad-J_s\big\{p_l\sin\Theta_l\big[4M_l^y+M_{l+1}^y+M_{l-1}^y(1-\delta_{l,0})\big]\big\}\\
&\quad+(1/\beta)(1+\ln\rho_l), \qquad \text{(A11)}
\end{aligned}
$$

where we have defined the following order parameters (OPs):

$$
\begin{aligned}
X_l&:=\langle s_l\rangle,\\
D_l&:=\langle q_l\rangle,\\
M_l^x&:=\langle p_l\cos\Theta_l\rangle,\\
M_l^y&:=\langle p_l\sin\Theta_l\rangle. \qquad \text{(A12)}
\end{aligned}
$$

Equation (A11) can be solved for $\rho_l(s_l,\Theta_l)$:

$$
\rho_l=e^{\beta\eta-1-\beta h_l}, \qquad \text{(A13)}
$$

where

$$
\begin{aligned}
h_l=&-s_l\{K[4X_l+X_{l+1}+X_{l-1}(1-\delta_{l,0})]+C[4D_l+D_{l+1}\\
&+D_{l-1}(1-\delta_{l,0})]+\mu_-+f_-(l)\}\\
&-q_l\{J[4D_l+D_{l+1}+D_{l-1}(1-\delta_{l,0})]+C[4X_l+X_{l+1}\\
&+X_{l-1}(1-\delta_{l,0})]+\mu_++f_+(l)\}\\
&-p_l\cos\Theta_l\big\{J_s\big[4M_l^x+M_{l+1}^x+M_{l-1}^x(1-\delta_{l,0})\big]\big\}\\
&-p_l\sin\Theta_l\big\{J_s\big[4M_l^y+M_{l+1}^y+M_{l-1}^y(1-\delta_{l,0})\big]\big\}
\end{aligned} \qquad \text{(A14)}
$$

is the effective single-site Hamiltonian for a lattice site in the lth layer.

The normalization $\mathrm{Tr}(\rho_l)=1$ yields

$$
e^{-\beta\eta+1}=\mathrm{Tr}(e^{-\beta h_l}) \qquad \text{(A15)}
$$

so that

$$
\rho_l=\frac{e^{-\beta h_l}}{\mathrm{Tr}(e^{-\beta h_l})}, \qquad \text{(A16)}
$$

where h_l is given by Eq. (A14).

Within the expression for h_l given in Eq. (A14) one has

$$
\begin{aligned}
\mathrm{Tr}e^{-\beta h_l}=&\,1+W_l(X_l,D_l;\mu_-,\mu_+,f_+(l),f_-(l),T)\\
&+R_l(X_l,D_l;\mu_-,\mu_+,f_+(l),f_-(l),T)I_0(\beta J_s\tilde{M}_l),
\end{aligned} \qquad \text{(A17)}
$$

where I_0 and I_1 are modified Bessel functions (see Sec. 9.6 in Ref. [48]) and

$$
\tilde{M}_l=\sqrt{\big[M_{l-1}^x(1-\delta_{l,0})+4M_l^x+M_{l+1}^x\big]^2+\big[M_{l-1}^y(1-\delta_{l,0})+4M_l^y+M_{l+1}^y\big]^2}. \qquad \text{(A18)}
$$

The functions $W(X_l,D_l;\mu_-,\mu_+,f_+(l),f_-(l),T)$ and $R(X_l,D_l;\mu_-,\mu_+,f_+(l),f_-(l),T)$ are given by

$$
\begin{aligned}
W_l(X_l,D_l;\mu_-,\mu_+,f_+(l),f_-(l),T)=&\exp\beta\{(J-C)[D_{l-1}(1-\delta_{l,0})+4D_l+D_{l+1}]+(C-K)[X_{l-1}(1-\delta_{l,0})+4X_l+X_{l+1}]\\
&+\mu_++f_+(l)-\mu_--f_-(l)\}
\end{aligned} \qquad \text{(A19)}
$$

and

$$
\begin{aligned}
R_l(X_l,D_l;\mu_-,\mu_+,f_+(l),f_-(l),T)=&\exp\beta\{(J+C)[D_{l-1}(1-\delta_{l,0})+4D_l+D_{l+1}]+(C+K)[X_{l-1}(1-\delta_{l,0})\\
&+4X_l+X_{l+1}]+\mu_++f_+(l)+\mu_-+f_-(l)\}.
\end{aligned} \qquad \text{(A20)}
$$

Using the definitions in Eq. (A12) the OPs are given by four coupled self-consistent equations:

$$X_l = \frac{-W_l + R_l I_0(\beta J_s \tilde{M}_l)}{1 + W_l + R_l I_0(\beta J_s \tilde{M}_l)} \tag{A21}$$

and

$$D_l = \frac{W_l + R_l I_0(\beta J_s \tilde{M}_l)}{1 + W_l + R_l I_0(\beta J_s \tilde{M}_l)}; \tag{A22}$$

M_l^x and M_l^y are given by

$$M_l^x = \frac{(1-\delta_{l,0})M_{l-1}^x + 4M_l^x + M_{l+1}^x}{\tilde{M}_l} \times \frac{R_l I_1(\beta J_s \tilde{M}_l)}{1 + W_l + R_l I_0(\beta J_s \tilde{M}_l)} \tag{A23}$$

and

$$M_l^y = \frac{(1-\delta_{l,0})M_{l-1}^y + 4M_l^y + M_{l+1}^y}{\tilde{M}_l} \times \frac{R_l I_1(\beta J_s \tilde{M}_l)}{1 + W_l + R_l I_0(\beta J_s \tilde{M}_l)} \tag{A24}$$

so that

$$M_l := \sqrt{\left(M_l^x\right)^2 + \left(M_l^y\right)^2} = \frac{R_l I_1(\beta J_s \tilde{M}_l)}{1 + W_l + R_l I_0(\beta J_s \tilde{M}_l)}. \tag{A25}$$

Since (M_l^x, M_l^y) and $\tilde{M}_l$ are invariant under rotation around the z axis, it is sufficient to consider only one of the two components. We choose a rotation such that $M_l^y = 0$ and $M_l^x > 0$. With this choice one has

$$\tilde{M}_l = (1-\delta_{l,0})M_{l-1}^x + 4M_l^x + M_{l+1}^x \tag{A26}$$

and

$$M_l = \sqrt{\left(M_l^x\right)^2 + \left(M_l^y\right)^2} = M_l^x = \frac{R_l I_1(\beta J_s \tilde{M}_l)}{1 + W_l + R_l I_0(\beta J_s \tilde{M}_l)}. \tag{A27}$$

In order to determine the equilibrium free energy given in Eq. (A9) we first rearrange the term $(1/\beta)\langle \ln \prod_{l=0}^{L-1} \rho_l^{\mathcal{N}} \rangle$ [see also Eq. (A10)]:

$$\begin{aligned}(1/\beta)\left\langle \ln \prod_{l=0}^{L-1} \rho_l^{\mathcal{N}} \right\rangle &= (\mathcal{N}/\beta)\left\langle \sum_{l=0}^{L-1} \ln \rho_l \right\rangle \\ &= (\mathcal{N}/\beta)\sum_{l=0}^{L-1}\left\langle \ln \frac{e^{-\beta h_l}}{\mathrm{Tr}e^{-\beta h_l}} \right\rangle \\ &= -\mathcal{N}\sum_{l=0}^{L-1}\langle h_l\rangle - (\mathcal{N}/\beta)\sum_{l=0}^{L-1}\langle \ln \mathrm{Tr}e^{-\beta h_l}\rangle,\end{aligned} \tag{A28}$$

where in the last step, using Eqs. (A17) and (A22), we can write $\mathrm{Tr}e^{-\beta h_l} = (1-D_l)^{-1}$.

Inserting ρ_l into Eq. (A9) with the choice $M_l^y = 0$ and $M_l^x > 0$ and taking into account Eq. (A28) one obtains the following mean field expression for the equilibrium free energy:

$$\begin{aligned}\phi/\mathcal{N} = \sum_{l=0}^{L-1}\Big\{ &\frac{K}{2}X_l[4X_l + X_{l+1} + X_{l-1}(1-\delta_{l,0})] \\ &+ \frac{J}{2}D_l[4D_l + D_{l+1} + D_{l-1}(1-\delta_{l,0})] \\ &+ \frac{C}{2}X_l[4D_l + D_{l+1} + D_{l-1}(1-\delta_{l,0})] \\ &+ \frac{C}{2}D_l[4X_l + X_{l+1} + X_{l-1}(1-\delta_{l,0})] \\ &+ \frac{J_s}{2}M_l^x\big[4M_l^x + M_{l+1}^x + M_{l-1}^x(1-\delta_{l,0})\big] \\ &+ (1/\beta)\ln(1-D_l)\Big\}.\end{aligned} \tag{A29}$$

Note that in the general case (i.e., for both M_l^y and M_l^x being nonzero) the contribution $\sum_{l=0}^{L-1}\frac{J_s}{2}M_l^y[4M_l^y + M_{l+1}^y + M_{l-1}^y(1-\delta_{l,0})]$ has to be added to the right-hand side of Eq. (A29).

In order to obtain the functional form of the expressions for the chemical potentials, first Eqs. (A21) and (A22) have to be solved for W_l and R_l. Then, by comparing these solutions with the definitions of W_l and R_l as in Eqs. (A19) and (A20), one finds

$$\begin{aligned}\mu_+ = &\frac{T}{2}\ln\left(D_l^2 - X_l^2\right) - T\ln 2 - T\ln(1-D_l) \\ &- \frac{T}{2}\ln[I_0(\beta J_s \tilde{M}_l)] - J[D_{l-1}(1-\delta_{l,0}) \\ &+ 4D_l + D_{l+1}] - C[X_{l-1}(1-\delta_{l,0}) \\ &+ 4X_l + X_{l+1}] - f_+(l)\end{aligned} \tag{A30}$$

and

$$\begin{aligned}\mu_- = &\frac{T}{2}\ln\frac{D_l + X_l}{D_l - X_l} - \frac{T}{2}\ln[I_0(\beta J_s \tilde{M}_l)] \\ &- C[D_{l-1}(1-\delta_{l,0}) + 4D_l + D_{l+1}] \\ &- K[X_{l-1}(1-\delta_{l,0}) + 4X_l + X_{l+1}] - f_-(l).\end{aligned} \tag{A31}$$

Finally, one can implicitly express the magnetization M_l in terms of X_l and D_l by using Eqs. (A21), (A22), and (A25):

$$\frac{X_l + D_l}{2} = \frac{M_l I_0(\beta J_s \tilde{M}_l)}{I_1(\beta J_s \tilde{M}_l)}. \tag{A32}$$

APPENDIX B: CHOICE OF THE COUPLING CONSTANTS FOR THE CASE OF ^{3}He-^{4}He MIXTURES

In this Appendix we provide the reasoning for the choice of the phase diagram in Fig. 4(c) as mentioned in Sec. II B. We start by reviewing the corresponding discussion in Ref. [33] about how, within the present model, for a suitable value of J_s the bulk phase diagram of a classical binary mixture with specific values of $(C_0/K_0, J_0/K_0)$ and for $J_s = 0$ (dotted curve in Fig. 23) transforms into that of ^{3}He-^{4}He mixtures. Figure 23 illustrates schematically this transformation. One has to find and to adopt a nonzero value of $J_s = J_s^0$ such that the critical

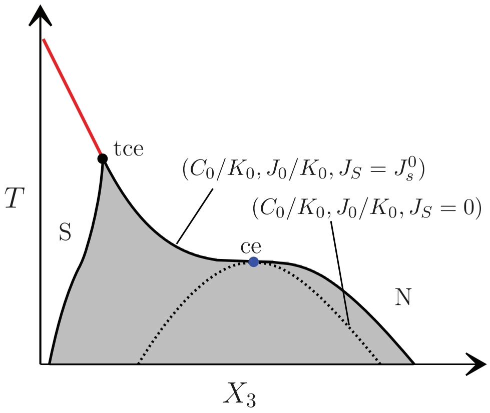

FIG. 23. Schematic representation of the transformation of the bulk phase diagram of a classical binary liquid mixture for fixed values of $(C_0/K_0,J_0/K_0)$ and $J_s = 0$ (the dotted curve) into that of ^{3}He-^{4}He mixtures with $J_s = J_s^0 \neq 0$ (solid curves). In a first step, for suitable, fixed values of $(C_0/K_0,J_0/K_0)$ and $J_s = 0$ one has the phase diagram of a classical binary mixture with ce as in Fig 4(a). In a second step, one has to find a nonzero value of $J_s = J_s^0$ (which produces the superfluid phase) such, that the critical end point ce of the phase diagram for $(C_0/K_0,J_0/K_0,J_s = 0)$, is in thermodynamic coexistence with a superfluid phase. For this new set of coupling constants $(C_0/K_0,J_0/K_0,J_s > J_s^0)$, the phase diagram with $(C_0/K_0,J_0/K_0,J_s = 0)$ lies in the two-phase region of the phase diagram with $(C_0/K_0,J_0/K_0,J_s > J_s^0)$.

end point ce of the phase diagram for $(C_0/K_0,J_0/K_0,J_s = 0)$ is in thermodynamic coexistence with a superfluid phase. This locates the critical end point ce on the right shoulder of the transformed phase diagram. Thus for $J_s > J_s^0$, the initial phase diagram for $(C_0/K_0,J_0/K_0,J_s = 0)$ (including its critical end point ce), lies in the two-phase region of the phase diagram for $(C_0/K_0,J_0/K_0,J_s > J_s^0)$ [37]. Although the phase diagram in Fig. 4(b) satisfies the above condition and captures the main features of the bulk phase diagram of ^{3}He-^{4}He mixtures, its shape near the tricritical end point tce differs from the experimental one (see Fig. 2). In particular, in the phase diagram in Fig. 4(b), upon lowering the temperature below T_{tce} along the path $X_3 = X_3^{\mathrm{tce}}$, the model mixture does not enter the two-phase region, as it is the case for the actual ^{3}He-^{4}He mixtures. Note that the experimental phase diagram schematically shown in Fig. 2 is drawn in the $(T,\mathcal{C}_3)$ plane. [The model phase diagram in the same $(T,\mathcal{C}_3)$ plane is shown in the inset of Fig. 4(b).] Furthermore, although the condition $J_s > J_s^0$ places the critical end point ce of the phase diagram with $(C_0/K_0,J_0/K_0,J_s = 0)$ into the two-phase region of the phase diagram with $(C_0/K_0,J_0/K_0,J_s > J_s^0)$, a certain residual, distorting influence of this critical end point ce on the wetting films may still be present, especially if ce lies near any of the two binodals of the demixing transitions of the transformed phase diagram [solid black lines in Figs. 4(b) and 4(c)]. In order to address this issue, after finding the necessary conditions for the coupling parameters leading to the desired topology, we have modified the values of $(C_0/K_0,J_0/K_0)$ with $J_s = J_s^0$ such, that the critical end point ce (which starts to shift into metastablity for $J_s = J_s^0$) moves deeply into the two-phase region of the transformed phase diagram. These considerations have led us to choosing the following choice for the coupling constants: $(C/K,J/K,J_s/K) = (1,9.10714,3.70107)$. The corresponding phase diagram is shown in Fig. 4(c).

[1] M. Krech and S. Dietrich, Phys. Rev. A **46**, 1922 (1992).
[2] R. Garcia and M. H. W. Chan, Phys. Rev. Lett. **83**, 1187 (1999).
[3] R. Garcia and M. H. W. Chan, Phys. Rev. Lett. **88**, 086101 (2002).
[4] A. Ganshin, S. Scheidemantel, R. Garcia, and M. H. W. Chan, Phys. Rev. Lett. **97**, 075301 (2006).
[5] M. Fukuto, Y. F. Yano, and P. S. Pershan, Phys. Rev. Lett. **94**, 135702 (2005).
[6] S. Rafaï, D. Bonn, and J. Meunier, Physica **386**, 31 (2007).
[7] A. Mukhopadhyay and B. M. Law, Phys. Rev. Lett. **83**, 772 (1999).
[8] A. Mukhopadhyay and B. M. Law, Phys. Rev. E **62**, 5201 (2000).
[9] M. E. Fisher and P. G. de Gennes, C. R. Seances Acad. Sci. Paris Ser. B **287**, 207 (1978).
[10] K. Binder, in *Phase Transitions and Critical Phenomena*, edited by C. Domb and J. L. Lebowitz (Academic Press, London, 1983), Vol. 8, p. 149.
[11] V. Privman, in *Finite Size Scaling and Numerical Simulation of Statistical Systems*, edited by V. Privman (World Scientific, Singapore, 1990), p. 1.
[12] H. Casimir, Proc. K. Ned. Akad. Wet. **51**, 793 (1948).
[13] M. Krech, *The Casimir Effect in Critical Systems* (World Scientific, Singapore, 1994).
[14] M. P. Nightingale and J. O. Indekeu, Phys. Rev. Lett. **54**, 1824 (1985).
[15] M. Krech and S. Dietrich, Phys. Rev. Lett. **66**, 345 (1991).
[16] M. Krech and S. Dietrich, Phys. Rev. A **46**, 1886 (1992).
[17] H. W. Diehl, in *Phase Transitions and Critical Phenomena*, edited by C. Domb and J. L. Lebowitz (Academic Press, London, 1986), Vol. 10, p. 75.
[18] J. G. Brankov, D. Danchev, and N. Tonchev, in *Theory of Critical Phenomena in Finite-Size Systems* (World Scientific, Singapore, 2000), Vol. 9, p. 125.
[19] R. Zandi, J. Rudnick, and M. Kardar, Phys. Rev. Lett. **93**, 155302 (2004).
[20] A. Maciołek and S. Dietrich, Europhys. Lett. **74**, 22 (2006).
[21] A. Maciołek, A. Gambassi, and S. Dietrich, Phys. Rev. E **76**, 031124 (2007).
[22] R. Zandi, A. Shackell, J. Rudnick, M. Kardar, and L. P. Chayes, Phys. Rev. E **76**, 030601(R) (2007).
[23] O. Vasilyev, A. Gambassi, A. Maciołek, and S. Dietrich, Europhys. Lett. **80**, 60009 (2007).
[24] O. Vasilyev, A. Gambassi, A. Maciołek, and S. Dietrich, Phys. Rev. E **79**, 041142 (2009).
[25] D. Dantchev and M. Krech, Phys. Rev. E **69**, 046119 (2004).
[26] A. Hucht, Phys. Rev. Lett. **99**, 185301 (2007).
[27] M. Hasenbusch, J. Stat. Mech. (2009) P07031.
[28] M. Hasenbusch, Phys. Rev. B **81**, 165412 (2010).
[29] J. P. Romagnan, J. P. Laheurte, J. C. Noiray, and W. F. Saam, J. Low Temp. Phys. **30**, 425 (1978).

[30] M. Blume, V. J. Emery, and R. B. Griffiths, Phys. Rev. A **4**, 1071 (1971).

[31] A. N. Berker and D. R. Nelson, Phys. Rev. B **19**, 2488 (1979).

[32] J. L. Cardy and D. J. Scalapino, Phys. Rev. B **19**, 1428 (1979).

[33] N. Farahmand Bafi, A. Maciołek, and S. Dietrich, Phys. Rev. E **91**, 022138 (2015).

[34] V. Dohm, J. Low Temp. Phys. **69**, 51 (1987).

[35] M. Galassi, J. Davies, J. Theiler, B. Gough, G. Jungman, P. Alken, M. Booth, and F. Rossi, *GNU Scientific Library Reference Manual*, Network Theory Ltd., 2009; library available online at http://www.gnu.org/software/gsl/.

[36] A. Maciołek, M. Krech, and S. Dietrich, Phys. Rev. E **69**, 036117 (2004).

[37] G. M. Bell and D. A. Lavis, *Statistical Mechanics of Lattice Models* (Springer, Chichester, 1989), Vol. 1.

[38] S. Dietrich, in *Phase Transitions and Critical Phenomena*, edited by C. Domb and J. L. Lebowitz (Academic Press, London, 1988), Vol. 12, p. 1.

[39] S. Dietrich, in *Phase Transitions in Surface Films 2*, edited by H. Taub, G. Torzo, H. J. Lauter, and S. C. Fain, Proceedings of the NATO ASI (Series B) (Plenum, New York, 1991), Vol. B 267, p. 391.

[40] R. Evans, J. Phys.: Condens. Matter **2**, 8989 (1990).

[41] M. Krech, Phys. Rev. E **56**, 1642 (1997).

[42] A. Gambassi, J. Phys: Conf. Ser. **161**, 012037 (2009).

[43] S. Dietrich and M. Napiórkowski, Phys. Rev. A **43**, 1861 (1991).

[44] K. Binder, D. Landau, and M. Müller, J. Stat. Phys. **110**, 1411 (2003).

[45] E. K. Riedel, Phys. Rev. Lett. **28**, 675 (1972).

[46] I. D. Lawrie and S. Sarbach, in *Phase Transitions and Critical Phenomena*, edited by C. Domb and J. L. Lebowitz (Academic Press, London, 1986), Vol. 9, p. 1.

[47] P. M. Chaikin and T. Lubensky, *Principles of Condensed Matter Physics* (Cambridge University Press, Cambridge, 1995).

[48] M. Abramowitz and I. A. Stegun, (eds.), *Handbook of Mathematical Functions* (Dover, New York, 1972).